Advancing precision oncology: insights from C-terminal FGFR2/3 truncations and MYC-driven mTOR inhibitor resistance

Yemelyanenko, J.

CHAPTER 5

C-TERMINAL TRUNCATION AND FUSION PARTNER DETERMINE ONCOGENICITY OF FGFR3

Julia Yemelyanenko*, Jinhyuk Bhin*, Eline van der Burg, Anne Paulien Drenth, Jessica K. Lee, Catrin Lutz, Lea Dörner, Ellen Wientjens, Sjoerd Klarenbeek, Ji-Ying Song, Hyeonjin Moon, Stefano Annunziato, Natalie Proost, Bjørn Siteur, Jeffrey S. Ross, Marieke van de Ven, Olaf van Tellingen, Shridar Ganesan, Lodewyk F. A. Wessels, Daniel Zingg# & Jos Jonkers#

*equal contribution
#co-corresponding author

Cancer Research, 2026 Mar 16; 86(6):1372-1391
https://doi.org/10.1158/0008-5472.CAN-24-2648

ABSTRACT

Genomic alterations affecting components of the fibroblast growth factor (FGF) signaling axis can trigger aberrant pathway activation and tumor development. Genomic truncation of the FGF receptor 2 (*FGFR2*) exon 18 (E18) disrupts the FGFR2 carboxy-terminal tail (C-tail), acting as a potent driver alteration across multiple tumor types. Here, we analyzed human oncogenomic datasets to reveal that E18 truncations are similarly prevalent in *FGFR3*, an *FGFR2* paralog. *FGFR3* E18 truncations primarily occurred due to rearrangements (REs) that involve transforming acidic coiled-coil containing protein 3 (*TACC3*), resulting in *FGFR3*$^{\Delta E18}$*-TACC3* gene fusions. In contrast to E18-truncated *FGFR2*, functional *in vitro* and *in vivo* examination of *Fgfr3* variants demonstrated that the truncation of *Fgfr3* E18 is insufficient to promote oncogenic activity in cell lines or in the lungs and mammary glands of mice. Only the combination of an *Fgfr3* E18 truncation with a RE partner gene that encodes a receptor-dimerizing domain resulted in the development of tumors, which were sensitive to FGFR inhibition. Overall, these findings suggest that patients with cancers that are positive for rearranged *FGFR3* resulting in E18 truncation and a fusion to dimerizing partners should be considered for FGFR-targeted therapies.

Significance

FGFR3, unlike its paralog FGFR2, requires both a C-terminal truncation and fusion to a partner gene that retains the expression of a dimerizing domain to effectively drive oncogenic signaling and tumorigenesis.

INTRODUCTION

Genomic alterations affecting components of the fibroblast growth factor (FGF) / FGF receptor (FGFR) signaling pathway are frequent in human cancer. In fact, approximately 7% of cancer patients across a wide variety of tumor types harbor alterations in *FGFR* genes [1–3]. Gene amplifications (~60%) are the most prevalent alterations, followed by activating mutations (~30%) and gene fusions/rearrangements (REs, ~10%; refs. [1,3]). Notably, the incidence of alterations in the individual *FGFR* genes varies in a tissue-specific manner [1–3]. *FGFR1* amplifications, present as part of a large 8p11 amplicon, are the most common *FGFR* aberrations, primarily observed in breast, urothelial, ovarian, and squamous cell lung carcinomas. *FGFR2* activating mutations and amplifications are prevalent in endometrial cancer, whereas *FGFR2* fusions are frequently found in cholangiocarcinoma. *FGFR3* is most commonly altered in urothelial bladder and upper urinary tract cancers, with activating mutations and gene fusions being predominant.

The pan-FGFR inhibitors (FGFRi) erdafitinib and futibatinib as well as the FGFR1–3 inhibitors pemigatinib and infigratinib have recently received regulatory approvals in several *FGFR*-altered indications, and further small-molecule FGFRi and other biologic agents targeting FGFRs are currently being evaluated in clinical trials [4]. However, only 20–40% of patients with solid *FGFR*-altered tumors show objective responses to FGFRi [4]. This underscores the need to discern which FGFR alterations are tumor-driving and thus amenable to targeted therapeutic strategies.

We recently uncovered truncation of exon 18 (E18) of *FGFR2* as a potent driver alteration in cancer, irrespective of specific fusion partners [5]. Our work showed that the carboxy (C)-terminal tail of FGFR2, encoded by E18, can be subjected to a plethora of genomic alterations that lead to its loss and the subsequent initiation of oncogenic transformation. These alterations include canonical in-frame fusions with 3'-partner genes, non-canonical REs, partial E1-E17 amplifications, E18 splice-acceptor-site mutations and E18-truncating mutations. Importantly, analysis of FGFRi clinical trial data revealed that patients with cancers containing C-terminally-truncating *FGFR2* variants show clinically meaningful responses, irrespective of the truncation variant type [5,6].

Cancer genomic profiling has identified recurrent breakpoints (BPs) within intron 17 (I17) and E18 of *FGFR3* that lead to the generation of C-terminally truncated FGFR3 [5,7,8]. Given the structural and functional similarities between FGFR2 and FGFR3 [9], we hypothesized that, comparably to FGFR2, the loss of the FGFR3 C-terminal tail may suffice to generate an oncogene. However, oncogenomic analysis and functional annotation of *FGFR3* alterations revealed that FGFR3, as opposed to its paralog FGFR2, requires both C-terminal truncation and a fusion partner with retained dimerizing capacity to convert to an oncogene.

RESULTS

FGFR3 E18 truncations in human cancer

To study human cancer-associated *FGFR3* alterations causing E18-truncation, we analyzed 249,570 pan-cancer targeted tumor sequencing profiles derived from Foundation Medicine Inc. (FMI). We identified 799 samples (0.32% incidence) across a broad range of tumor indications that contain *FGFR3* alterations potentially resulting in the expression of *FGFR3* transcripts devoid of E18 (**Fig. 1A**; Supplementary Data S1). These could be classified into two mutually exclusive categories comprising *FGFR3* E18-truncating mutations (*n*=98, 12.3% of the 799 tumors; **Fig. 1A**; Supplementary Fig. S1A and S1B) and structural REs within the *FGFR3* locus (*n*=701, 87.7%). The REs resulted in canonical in-frame fusions with other partner genes (*n*=318, 39.8%) or non-canonical REs in which the reading frame of the partner gene could not be defined (frame-unknown; *n*=317, 39.7%), the partner sequence had its origin in intergenic space (*n*=36, 4.5%), the partner gene was out-of-strand (*n*=29, 3.6%) and internal gene REs (*n*=1, 0.1%). In most cases, *FGFR3* was located upstream of its RE partner (*n*=674, 96.1%), REs predominantly occurred intrachromosomally within chromosome 4 (*n*=648, 92.4%) and the majority of the *FGFR3* BPs were located either in I17 (*n*=410, 58.5%) or E18 (*n*= 283, 40.2%). Notably, transforming acidic coiled-coil containing protein 3 (*TACC3*) was the single most recurrent RE partner gene of *FGFR3* (*n*=574, 81.9%). This finding contrasted with the diverse RE partners observed for *FGFR2* [5].

We next analyzed WGS profiles of 4,863 metastatic solid tumors from the Hartwig Medical Foundation (HMF; ref. [10]) and found 32 tumors (0.66% incidence) that had structural REs affecting *FGFR3* (Supplementary Data S2). Consistent with the results obtained from the FMI cohort, this analysis revealed a significant enrichment of RE BPs in I17 and E18 of *FGFR3* (*n*=19, 59.4%) (**Fig. 1B** and **C**). Amongst these, we found 3 in-frame (15.8%), 14 frame-unknown (73.7%), and 2 intergenic space (10.5%) REs (**Fig. 1D**). 10 samples containing *FGFR3* REs in I17 or E18 concomitantly presented full-length or partial amplifications of the *FGFR3* locus (*FGFR3^{amp}*; 43.8%; **Fig. 1D**).

Figure 1. *FGFR3* E18 truncations in human cancer.

A, Analysis of 799 samples (0.32% incidence) carrying potential *FGFR3*-E18 truncations identified among 249,570 pan-cancer diagnostic hybrid-capture panel-seq profiles from FMI. These samples include *FGFR3* REs with BPs at the C-terminal tail, E17/18 or I16/17 and/or *FGFR3* E18-truncating mutations. *FGFR3* REs consist of I17 in-frame fusions (*n*=318, 39.8% incidence among 799 samples with potential *FGFR3*-E18 alterations), frame-unknown REs (*n*=317, 39.7% incidence), intergenic space REs (*n*=36, 4.5% incidence), out-of-strand REs (*n*=29, 3.6% incidence), internal RE (*n*=1, 0.1% incidence) and/or *FGFR3* E18-truncating mutations (mut; *n*=98, 12.3% incidence). Tumor type, *FGFR3* amplification status (*FGFR3*^{amp}; E1-E18 full-length and E1-E17 partial amplifications), and BP location of *FGFR3* and its corresponding RE partners are indicated. *FGFR3* REs with *TACC3* are highlighted. **B**, BPs generating *FGFR3* genomic REs identified in 32 out of 4,863 analyzed WGS profiles from the HMF cohort on metastatic solid tumors [10]. BP density was calculated using a 300 bp sliding window. The blue bars show BPs. Corresponding exon count and protein domains are indicated. Ig, immunoglobulin-like domains; TM, transmembrane domain; Tyr KD, tyrosine kinase domain; CT, C-terminal tail. **C,** Normalized frequency (top panel) and enrichment significance (*P* values, bottom panel) of *FGFR3* genomic RE BPs identified in 32 WGS profiles from the HMF cohort in each exon/intron. BP frequency was normalized by the kilobase of feature (exon/intron) length and the total number of BPs in *FGFR3*. *P* values were calculated with one-tailed binomial tests. **D**, *FGFR3* RE types and full-length and partial amplifications found in 32 WGS profiles from HMF. BP location of

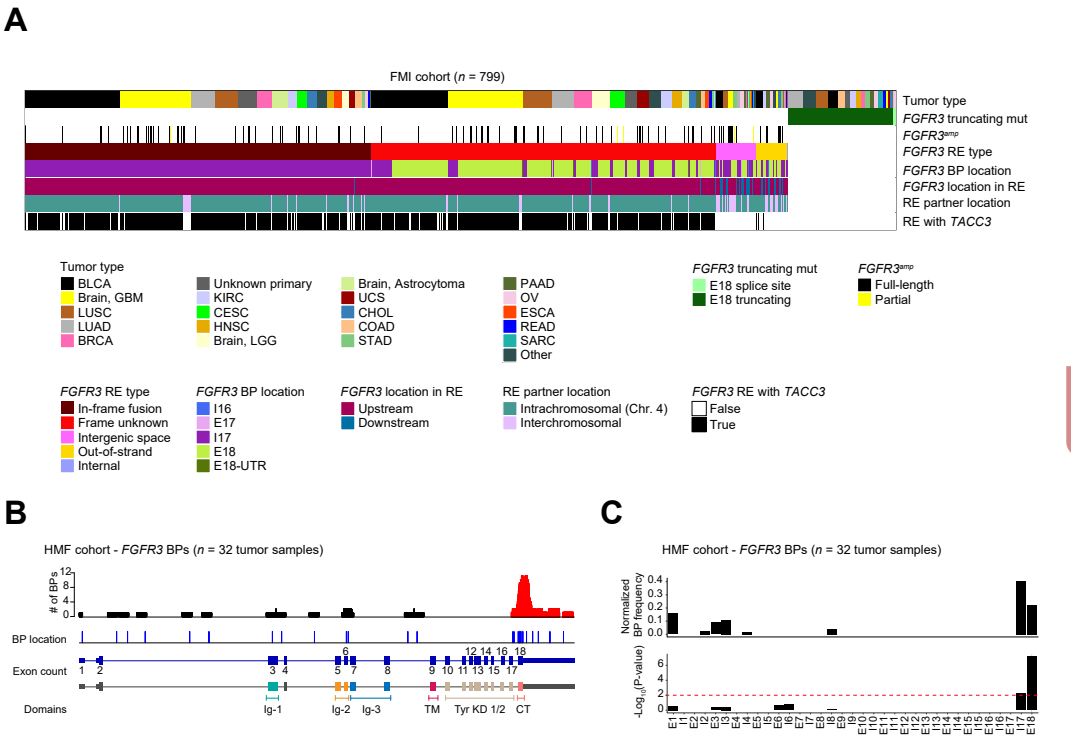

FGFR3 and its corresponding RE partners are indicated. RNA support indicates evidence for *FGFR3* REs in matching RNA-seq profiles, and cases with predicted C-terminal truncation are highlighted. Empty fields, no RNA-seq data available. BLCA, bladder urothelial carcinoma; GBM, glioblastoma multiforme; LUSC, lung squamous cell carcinoma; LUAD, lung adenocarcinoma; BRCA, breast invasive carcinoma; KIRC, kidney renal clear cell carcinoma; CESC, cervical squamous cell carcinoma and endocervical adenocarcinoma; HNSC, head and neck squamous cell carcinoma; LGG, low-grade glioma; UCS, uterus carcinosarcoma; CHOL, cholangiocarcinoma; COAD, colon adenocarcinoma; STAD, stomach adenocarcinoma; PAAD, pancreatic adenocarcinoma; OV, ovarian serous cystadenocarcinoma; ESCA, oesophageal carcinoma; READ, rectum adenocarcinoma; SARC, sarcoma; THCA, papillary thyroid carcinoma.

Expression of E18-truncating *FGFR3* variants

Next, we evaluated matching RNA-seq profiles that were available for 27 out of the 32 tumor samples with WGS profiles that revealed structural REs in *FGFR3* (**Fig. 1D** and **2A-E**; Supplementary Fig. S1C). For 9 samples predicted to have in-frame, out-of-strand, or intergenic space REs, we could confirm the expression of the respective *FGFR3* RE types. Furthermore, 12 out of the 14 tumors with frame-unknown *FGFR3* REs (85.7%) showed in-frame REs at the transcript level (**Fig. 1D** and **2B**). Interestingly, in most cases where BPs were observed in *FGFR3* I17 or E18, transcripts showed E18-skipping with junction reads connecting E17 to the RE partner genes (**Fig. 2A** and **C**; Supplementary Fig. S1C). In three cases with an *FGFR3* BP within E18, we observed expression of transcripts that show in-frame splicing originating within E18 and bridging to the RE partner (**Fig. 2A, B, D** and **E**; E18 partial retention in **Fig. 2A**, in blue). These transcripts encoded FGFR3 derivates devoid of a large portion of the C-terminal tail, thus likely resulting in a dysfunctional C-tail reminiscent of full E18 truncation.

In sum, we showed that genomic REs in human tumors cause the expression of *FGFR3* transcripts which either completely or partially lack E18 (*FGFR3*$^{\Delta E18}$), consequently resulting in dysfunctional C-terminal tails. Based on these findings, we propose that the frame-unknown REs encountered in the FMI cohort (**Fig. 1A**) may likewise encode in-frame transcripts.

Figure 2. Expression of E18-truncated *FGFR3* variants.

A, Overview of the BP locations on the C-terminal tail of *FGFR3* analyzed by WGS and the resulting transcripts (indicated by labels corresponding to each BP location) analyzed by matched RNA-seq data, from the HMF cohort. In red, transcripts lacking E17–E18 spanning reads which results in complete E18 skipping on RNA level; in blue, transcripts retaining a fraction of E18 comprised of the 5' exonic fragment prior to their corresponding BP; in black, transcripts with full E18 retention. **B**, Sashimi plot showing *FGFR3* read coverage and junction reads of the HMF sample CPCT022410009 (BRCA). *FGFR3*-E18 coding sequence (CDS) to *TACC3*-I5 frame-unknown RE identified with WGS and *FGFR3*-E18 to *TACC3*-E6 in-frame fusion found with RNA-seq. **C,** Sashimi plot showing *FGFR3* read coverage and junction reads of the HMF sample CPCT02050356 (BLCA). An in-frame *FGFR3*-I17 RE to *JAKMIP1*-I3 identified with WGS and an in-frame fusion *FGFR3*-E17 to *JAKMIP1*-E4 confirmed with RNA-seq. **D,** Sashimi plot showing *FGFR3* read coverage and junction reads of the HMF sample CPCT02020277 (BLCA). *FGFR3*-E18 coding sequence (CDS) RE to *TACC3*-E11 CDS identified with WGS and *FGFR3*-E18 to *TACC3*-E11 in-frame fusion confirmed with RNA-seq. **E,** Sashimi plot showing *FGFR3* read coverage and junction reads of the HMF sample CPCT02040255 (LUSC/LUAD). *FGFR3*-E18 CDS RE to intergenic space identified with WGS and *FGFR3*-E18 to intergenic region junctions found with RNA-seq. Green arrows indicate BPs identified with WGS.

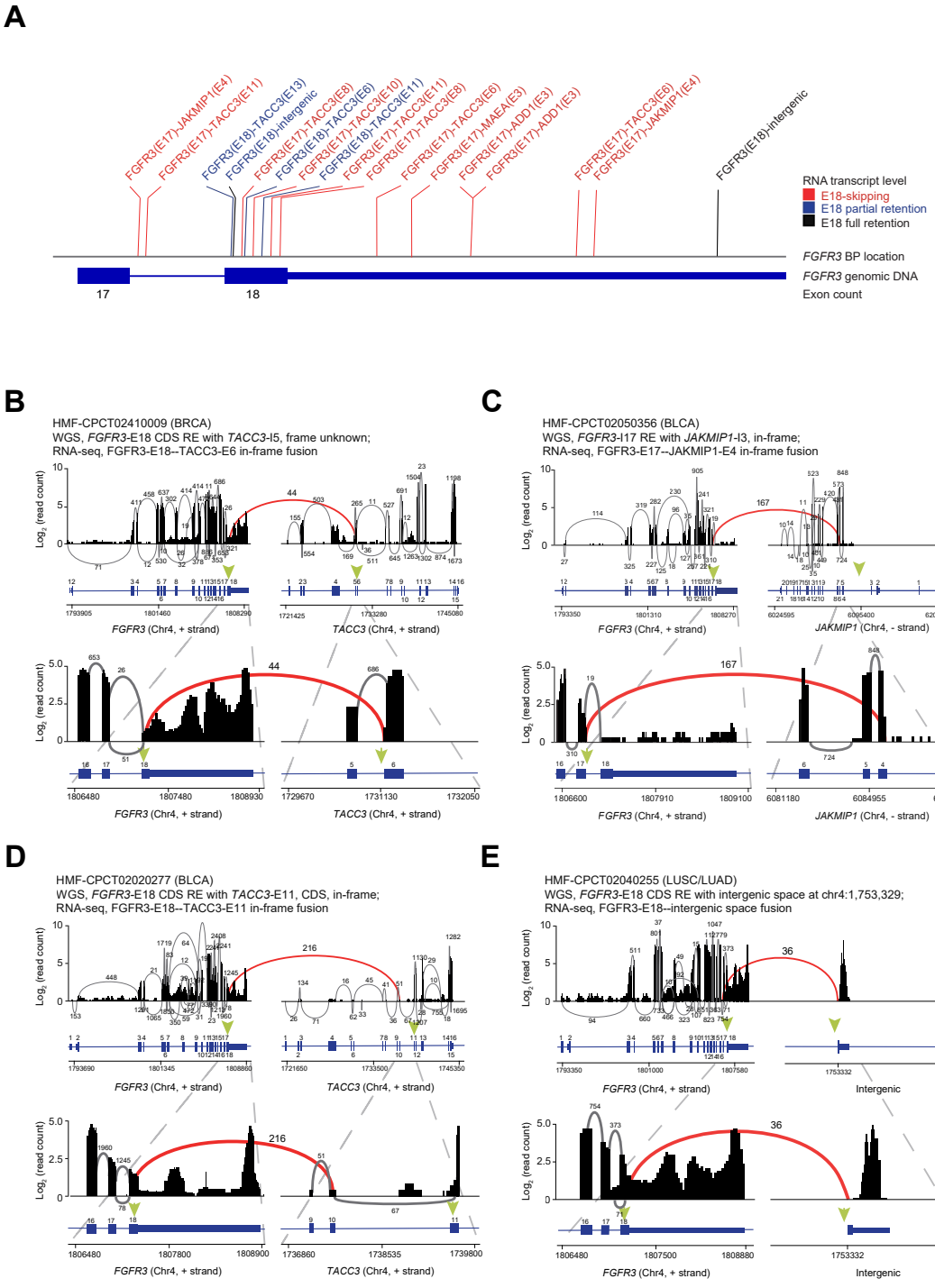
A
FGFR3(E17)-JAKMIP1(E4)
FGFR3(E17)-TACC3(E11)
FGFR3(E18)-TACC3(E13)
FGFR3(E18)-intergenic
FGFR3(E17)-TACC3(E8)
FGFR3(E18)-TACC3(E6)
FGFR3(E18)-TACC3(E10)
FGFR3(E17)-TACC3(E11)
FGFR3(E17)-TACC3(E11)
FGFR3(E17)-TACC3(E8)
FGFR3(E17)-TACC3(E6)
FGFR3(E17)-MAEA(E3)
FGFR3(E17)-ADD1(E3)
FGFR3(E17)-ADD1(E3)
FGFR3(E17)-TACC3(E6)
FGFR3(E17)-JAKMIP1(E4)
FGFR3(E18)-intergenic
RNA transcript level
E18-skipping
E18 partial retention
E18 full retention
FGFR3 BP location
FGFR3 genomic DNA
Exon count
17
18
B
HMF-CPCT02410009 (BRCA)
WGS, FGFR3-E18 CDS RE with TACC3-I5, frame unknown;
RNA-seq, FGFR3-E18--TACC3-E6 in-frame fusion
Log2 (read count)
FGFR3 (Chr4, + strand)
TACC3 (Chr4, + strand)
C
HMF-CPCT02050356 (BLCA)
WGS, FGFR3-I17 RE with JAKMIP1-I3, in-frame;
RNA-seq, FGFR3-E17--JAKMIP1-E4 in-frame fusion
Log2 (read count)
FGFR3 (Chr4, + strand)
JAKMIP1 (Chr4, - strand)
D
HMF-CPCT02020277 (BLCA)
WGS, FGFR3-E18 CDS RE with TACC3-E11, CDS, in-frame;
RNA-seq, FGFR3-E18--TACC3-E11 in-frame fusion
Log2 (read count)
FGFR3 (Chr4, + strand)
TACC3 (Chr4, + strand)
E
HMF-CPCT02040255 (LUSC/LUAD)
WGS, FGFR3-E18 CDS RE with intergenic space at chr4:1,753,329;
RNA-seq, FGFR3-E18--intergenic space fusion
Log2 (read count)
FGFR3 (Chr4, + strand)
Intergenic

FGFR3 RE partners are enriched for proteins with self-interacting capacity

Next, we classified the RE partner genes detected in the FMI cohort in more detail. *TACC3* was the single most recurrent partner gene, observed in 574 (85.3%) of all tumors carrying *FGFR3* E18-truncating REs (**Fig. 3A**; Supplementary Data S1). Intergenic space REs were the second most frequent (3.3%), while other known fusion partner genes were much less common (<2.0% each). Importantly, 94.8% of the proteins encoded by the RE partners contained self-interacting domains (**Fig. 3B**). The coiled-coil (CC) domain was found most frequently (90.5%), but other self-interacting domains, such as the HMG-box, SET, PWWP and Class II Aldolase domains, were also encountered (**Fig. 3B**; Supplementary Table S2). The ability to self-interact and the presence of CC domains was significantly enriched across the FGFR3 fusion partners as compared to the human proteome (**Fig. 3C** and **D**).

Previous research examining *FGFR3*$^{\Delta E18}$*-TACC3* fusions has predominantly relied on small cancer patient cohorts limited to specific tissue types [11,12]. In contrast, the extensive FMI data cohort used within this study allowed for detailed and unbiased analysis of the REs between *FGFR3*$^{\Delta E18}$ and *TACC3*. The 3'-BPs in *FGFR3* were mainly located in I17 and E18, whereas the 5'-BPs in *TACC3* were more diversely distributed across several introns and exons, particularly I10, I9 and I7 (**Fig. 3E** and **F**). Most *FGFR3*$^{\Delta E18}$*-TACC3* fusions contained *TACC3* E11-E16, which encode two C-terminal CC domains (**Fig. 3E** and **F**). Together, these data suggested that the dimerizing capacity of the RE partners may be a relevant feature of oncogenic FGFR3$^{\Delta E18}$ fusions.

Fgfr3$^{\Delta E18}$*-Tacc3* fusion induces oncogenic signaling and *in vitro* transformation

FGFR3-TACC3 fusions have been identified in several tumor types [1,11], most commonly in cancers of the brain [1,12–16], urinary tract [1,17], lung [1,18–22], and breast [23–25], in line with our comprehensive genomic analyses (**Fig. 1A** and **D**; Supplementary Data S1 and S2). Previous studies using mouse models of glioblastoma [13,15] and lung cancer [18] have shown that these fusions can act as potent oncogenes. However, the exact molecular mechanisms underlying their oncogenicity have remained incompletely understood.

To investigate the signaling pathways induced by FGFR3$^{\Delta E18}$ and FGFR3$^{\Delta E18}$-TACC3 fusions, we expressed *GFP*, full-length murine *Fgfr3* (*Fgfr3*^{FL}), *Fgfr3* lacking E18 (*Fgfr3*$^{\Delta E18}$), *Fgfr3*^{FL} fused to *Tacc3* (*Fgfr3*^{FL}*-Tacc3*), or *Fgfr3*$^{\Delta E18}$*-Tacc3* (Supplementary Methods S1) in NMuMG mouse mammary epithelial cells, with *Fgfr3*$^{\Delta E18}$*-Tacc3* corresponding to *FGFR3-TACC3* fusions observed in the clinic. The *TACC3* BP in *FGFR3-TACC3* frequently locates to I7, resulting in a partial *TACC3* transcript encoded by E8-E16 (**Fig. 3E, F** and **4A**). The corresponding murine *Tacc3* sequence that was used in the *Fgfr3* constructs consists of E7-E16. All constructs were expressed at comparable levels across engineered cell lines (**Fig. 4A**; Supplementary Fig. S2A). During serum starvation, expression of the *Fgfr3*$^{\Delta E18}$*-Tacc3* fusion resulted in marked baseline activation of FGFR3 and the mTOR signaling pathway effector proteins,

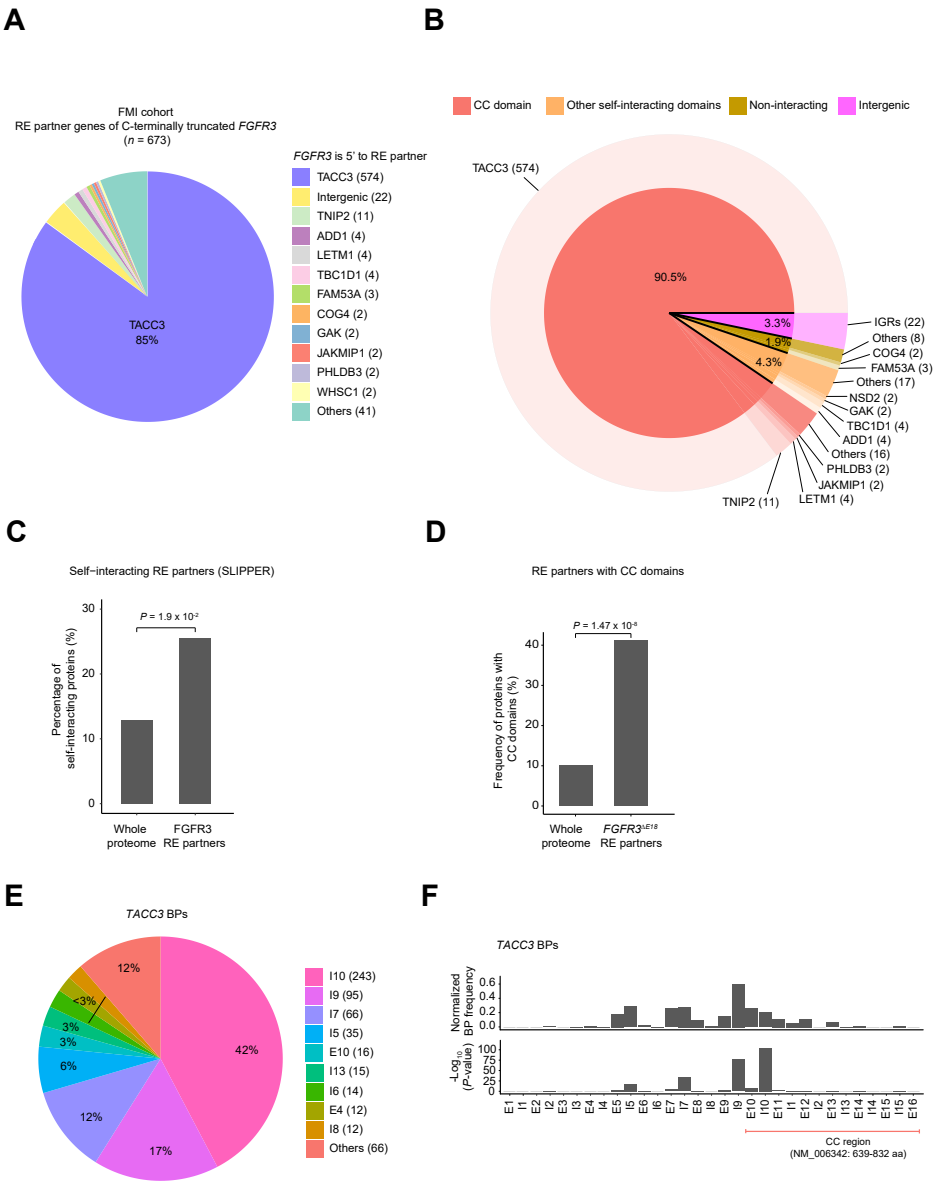

Figure 3. *FGFR3* RE partners are enriched for proteins with self-interacting capacity.

A, Recurrence of RE partners of C-terminally truncated *FGFR3* identified in the FMI cohort (*n*=673 tumors). **B**, Recurrence of *FGFR3* RE partners from (**A**) grouped by the presence or absence of self-interacting domains. Full list of RE partners and their corresponding self-interacting domains is disclosed in Supplementary Table S2. IGRs, intergenic regions; CC, coiled-coil. **C,** Frequency comparison between *FGFR3* RE partners that contain self-interacting domains and result in E18 truncation, based on the SLIPPER algorithm [27]. **D,** Frequency of proteins with CC domains among the E18-truncated *FGFR3* (21 out of 51) RE partners identified in the FMI cohort versus the human proteome (1993 out of 18975). *P* values were calculated with a two-tailed Fisher's exact test. **E**, Pie chart displaying the frequency of BPs in each exon/intron of *TACC3* identified in the 574 *FGFR3*$^{\Delta E18}$-*TACC3* fusions found in the FMI cohort. **F**, Normalized frequency (top panel) and enrichment significance (*P* values, bottom panel) of *TACC3* genomic RE BPs identified in (**E**). BP frequency was normalized by the kilobase of feature (exon/intron) length and total number of BPs. *P* values were calculated with a binomial test. Exons encompassing the CC region are indicated.

as evidenced by phosphorylation of FGFR3, RPS6, EIF4E, EIF4EBP1, EIF4B and stabilization of MYC. In contrast, all other *Fgfr3* variants tested showed no baseline activity (**Fig. 4B** and **C**). Stimulation with FGF-8b enhanced FGFR signaling via the mTOR axis in all FGFR3 variants (**Fig. 4B** and **C**). Similarly, activation of MAPK signaling hallmarked by the phosphorylation of ERK1/2 was predominantly induced through FGF-8b (**Fig. 4B** and **C**). Ligand-independent phosphorylation of STAT1, STAT3, FRS2 and PLCγ occurred exclusively in *Fgfr3*$^{\Delta E18}$*-Tacc3*-expressing cells and was further boosted upon stimulation with FGF-8b (**Fig. 4C** and **D**). Treatment of cells with the pan-FGFRi fexagratinib [26] as well as the clinically approved pan-FGFRi erdafitinib and futibatinib [4], suppressed FGFR3$^{\Delta E18}$-TACC3 signaling (**Fig. 4B-D**; Supplementary Fig. S2B-S2D), indicating that the constitutive activity of the FGFR3$^{\Delta E18}$-TACC3 fusion relies on canonical FGFR3 kinase domain function.

Next, we assessed the transforming capacity of FGFR3 fusion variants *in vitro*. First, we made use of a 3D soft agar growth assay to measure cellular transformation in an anchorage-independent manner [28]. In line with its enhanced baseline signaling capacity, *Fgfr3*$^{\Delta E18}$*-Tacc3*-expressing NMuMG cells showed considerable soft agar colony formation, as opposed to *GFP*, *Fgfr3*^{FL}, *Fgfr3*$^{\Delta E18}$ and *Fgfr3*^{FL}*-Tacc3* cells, which showed only marginal anchorage-independent growth (**Fig. 4E**; Supplementary Fig. S2E). These results were in striking contrast to what we previously observed for FGFR2, where loss of the C-terminal tail alone was sufficient to promote transformation and anchorage-independent growth of NMuMG cells [5]. We next expanded the functional evaluation to the Ba/F3 murine pro-B cell line that depends on IL-3 for survival and proliferation [29]. Consistent with our findings in NMuMG cells, only *Fgfr3*$^{\Delta E18}$*-Tacc3*-expressing Ba/F3 cells were able to proliferate during IL-3 withdrawal (**Fig. 4F**; Supplementary Fig. S2F and S2G). The kinase-dead *Fgfr3*$^{\Delta E18}$*-K502R-Tacc3* variant failed to promote IL-3-independent Ba/F3 cellular growth (**Fig. 4F**; Supplementary Fig. S2F and S2G) or activate oncogenic signaling in NMuMG cells with and without FGF-8b stimulation (Supplementary Fig. S2H and S2I), underscoring the critical role of kinase domain activity in driving oncogenicity of the FGFR3$^{\Delta E18}$-TACC3 fusion [13,30].

Together, these data established that loss of the FGFR3 C-terminal tail is required yet insufficient to promote oncogenic signaling and anchorage- or IL-3-independent growth. In contrast, C-terminal truncation and fusion to a partner containing a self-interacting domain, such as TACC3, is required for full oncogenic transformation of FGFR3.

Impaired internalization does not define FGFR3$^{\Delta E18}$-TACC3-driven transformation

Receptor tyrosine kinase (RTK) signaling is often negatively regulated through ligand-induced receptor internalization and subsequent lysosomal degradation, which limits signaling duration and intensity [31,32]. To assess whether impaired internalization contributes to FGFR3$^{\Delta E18}$-TACC3 oncogenicity, we evaluated receptor trafficking using HALO-tagged FGFR3 variants and the SPIDA assay [33]. NMuMG cells expressing *HALO-Fgfr3* variants (Supplementary Fig. S3A) were sequentially labeled with a cell-impermeable

fluorescent HaloTag ligand (AF660-HTL) followed by a cell-permeable fluorescent ligand (TMR-HTL), and fluorescence intensities of both ligands were subsequently quantified by FACS (**Fig. 4G**; Supplementary Fig. S3B). The relative abundance of FGFR3 at the plasma membrane versus the intracellular compartment was determined over time during FGF-8b stimulation using the SPIDA quantification framework [33] (**Fig. 4H** and **I**). As expected, HALO-FGFR3^{FL} underwent ligand-induced internalization upon FGF-8b stimulation, accompanied by only a modest increase in intracellular signal, consistent with receptor degradation following endocytosis (**Fig. 4G-I**). In contrast, the kinase-dead HALO-FGFR3^{FL}-K502R variant failed to internalize (**Fig. 4G** and **H**), underscoring the requirement for kinase activity in this process. Notably, none of the other HALO-tagged FGFR3 variants, including the FGFR3$^{\Delta E18}$-TACC3 fusion, displayed internalization upon ligand stimulation (**Fig. 4G** and **H**). This aligns with the fact that YXXΦ clathrin-mediated endocytosis motif [31] is located within E18 and therefore absent in truncated variants. While impaired internalization may contribute to sustained surface accumulation and aberrant signaling, it is not sufficient to drive transformation, as FGFR3$^{\Delta E18}$ alone – despite lacking the capacity to internalize (**Fig. 4G** and **H**) – did not induce oncogenic signaling (**Fig. 4B-D**; Supplementary Fig. S2B-S2D), provoke anchorage-independent 3D growth in NMuMG cells (**Fig. 4E**; Supplementary Fig. S2E), or confer IL-3-independent proliferation in Ba/F3 cells (**Fig. 4F**).

Fgfr3$^{\Delta E18}$-Tacc3 fusions drive mouse lung and mammary tumorigenesis

Our *in vitro* findings prompted us to evaluate the *in vivo* oncogenic capacity of the different *Fgfr3* variants using somatic mouse modeling. To this end, we employed two different lentiviral delivery systems to the mouse lung and mammary gland, representing two human organ sites where *FGFR3$^{\Delta E18}$-TACC3* fusions are recurrently detected in cancer (**Fig. 1A** and **D**; Supplementary Data S1 and S2).

FGFR3$^{\Delta E18}$-TACC3 fusions are found in 0.14-2.1% of non-small cell lung cancers (NSCLC) [7,8,19]. The FMI cohort contained 87 NSCLC cases with *FGFR3$^{\Delta E18}$-TACC3* REs, of which 48 were diagnosed as lung squamous cell carcinoma (LUSC) and 39 as lung adenocarcinoma (LUAD) (**Fig. 1A**; Supplementary Data S1). The HMF cohort contained one NSCLC case with an *FGFR3$^{\Delta E18}$*-TACC3 fusion (**Fig. 1D** and **2E**; Supplementary Data S2). *TP53* missense mutations are the most prevalent co-alterations in *FGFR3*-mutated lung cancer [8,18]. Consistently, 87% of all the LUSC/LUAD tumors in the FMI cohort with *FGFR3* alterations presented co-occurring *TP53* mutations (*n*=107 out of 123; Supplementary Fig. S4A).

To model the oncogenic potential of the different *Fgfr3* variants in the lung, we performed intratracheal intubation and delivery of lentiviral vectors encoding *Fgfr3-P2A-Cre* into wild-type and *Trp53$^{F/F}$* mice (**Fig. 5A**). In wild-type mice, *Fgfr3$^{\Delta E18}$-Tacc3-P2A-Cre* expression resulted in lung tumor formation in a fraction of the intubated animals, as opposed to no tumor formation in the *Fgfr3^{FL}-P2A-Cre*, *Fgfr3$^{\Delta E18}$-P2A-Cre* or *Fgfr3^{FL}-Tacc3-P2A-Cre* cohorts (**Fig. 5B**). Histopathological examination of the lungs intubated with *Fgfr3$^{\Delta E18}$-Tacc3-P2A-Cre*

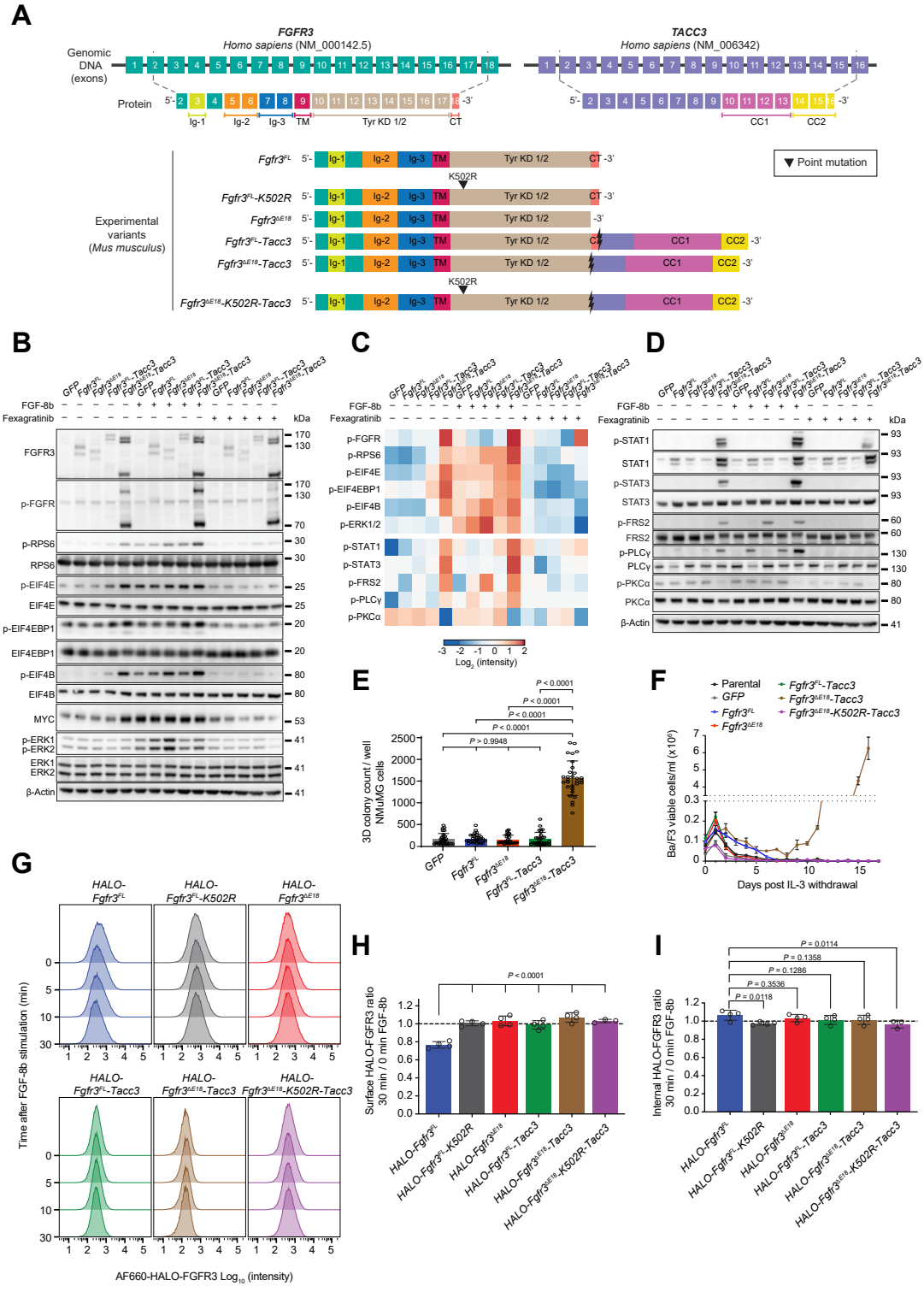
A
FGFR3
Homo sapiens (NM_000142.5)
TACC3
Homo sapiens (NM_006342)
Genomic DNA (exons)
Protein
Ig-1
Ig-2
Ig-3
TM
Tyr KD 1/2
CT
CC1
CC2
Point mutation
Experimental variants (Mus musculus)
Fgfr3FL
Fgfr3FL-K502R
Fgfr3ΔE18
Fgfr3FL-Tacc3
Fgfr3ΔE18-Tacc3
Fgfr3ΔE18-K502R-Tacc3
K502R
B
FGF-8b
Fexagratinib
kDa
FGFR3
p-FGFR
p-RPS6
RPS6
p-EIF4E
EIF4E
p-EIF4EBP1
EIF4EBP1
p-EIF4B
EIF4B
MYC
p-ERK1
p-ERK2
ERK1
ERK2
β-Actin
C
p-FGFR
p-RPS6
p-EIF4E
p-EIF4EBP1
p-EIF4B
p-ERK1/2
p-STAT1
p-STAT3
p-FRS2
p-PLCγ
p-PKCα
Log2 (intensity)
D
p-STAT1
STAT1
p-STAT3
STAT3
p-FRS2
FRS2
p-PLCγ
PLCγ
p-PKCα
PKCα
β-Actin
E
3D colony count / well NMuMG cells
P < 0.0001
P > 0.9948
F
Parental
GFP
Fgfr3FL
Fgfr3ΔE18
Fgfr3FL-Tacc3
Fgfr3ΔE18-Tacc3
Fgfr3ΔE18-K502R-Tacc3
Baf3 viable cells/ml (x10⁶)
Days post IL-3 withdrawal
G
HALO-Fgfr3FL
HALO-Fgfr3FL-K502R
HALO-Fgfr3ΔE18
HALO-Fgfr3FL-Tacc3
HALO-Fgfr3ΔE18-Tacc3
HALO-Fgfr3ΔE18-K502R-Tacc3
Time after FGF-8b stimulation (min)
AF660-HALO-FGFR3 Log10 (intensity)
H
Surface HALO-FGFR3 ratio 30 min / 0 min FGF-8b
P < 0.0001
I
Internal HALO-FGFR3 ratio 30 min / 0 min FGF-8b
P = 0.0114
P = 0.1358
P = 0.1286
P = 0.3536
P = 0.0118

Figure 4. *Fgfr3$^{\Delta E18}$-Tacc3* fusion induces oncogenic signaling and *in vitro* transformation.

A, Schematic representation of the genomic DNA and the resulting mature peptide of human *FGFR3* and *TACC3*. Protein domains of cloned mouse *Fgfr3* variants are indicated. Complete nucleotide and AA sequences for *Fgfr3$^{\Delta E18}$-Tacc3* are disclosed in Supplementary Methods S1. **B,** Western blots showing expression and phosphorylation of indicated proteins in 24 hr serum-starved NMuMG cells stably expressing *GFP*, *Fgfr3^{FL}*, *Fgfr3$^{\Delta E18}$*, *Fgfr3^{FL}-Tacc3*, or *Fgfr3$^{\Delta E18}$-Tacc3* and treated for 10 min with 20 ng/ml FGF-8b and/or for 3 hr with 1 μM fexagratinib. β-Actin was run as sample processing control and blots were stained with Ponceau S to ensure equal loading of total protein. Molecular weights of protein marker bands are indicated in kilodalton (kDa). **C,** Quantifications of indicated phosphoprotein band intensities based on Western blots in (**B, D**). Phospho band intensities were normalized to their individual lane backgrounds and to their corresponding total protein band intensities and β-Actin bands. **D,** Western blots generated as in (**B**), showing expression and phosphorylation of additional proteins. β-Actin is duplicated from (**B**). **E,** Colony quantifications of 3D soft agar colony formation assays using NMuMG cells stably expressing *GFP*, *Fgfr3^{FL}*, *Fgfr3$^{\Delta E18}$*, *Fgfr3^{FL}-Tacc3*, or *Fgfr3$^{\Delta E18}$-Tacc3* and grown for 20 days. Data are represented as mean ± SD of *n*=30 independent replica from 5 individual experiments. **F,** Growth rates of parental and Ba/F3 cells stably expressing *GFP*, *Fgfr3^{FL}*, *Fgfr3$^{\Delta E18}$*, *Fgfr3^{FL}-Tacc3*, *Fgfr3$^{\Delta E18}$-Tacc3*, or *Fgfr3$^{\Delta E18}$-K502R-Tacc3* upon IL-3 withdrawal. Data are represented as mean ± SEM of *n*=3 independent replica from 1 representative experiment. Assay was performed at least 3 independent times. **G-I,** FACS to quantify HALO-FGFR3 internalization in serum-deprived NMuMG cells expressing indicated *HALO-Fgfr3* variants using the SPIDA assay [33]. Cells were treated with 20 ng/ml FGF-8b for 5, 10 or 30 min and sequentially labeled with cell membrane impermeable HaloTag ligand (HTL)-AF660 and with permeable HTL-TMR. AF660-HALO-FGFR3 (**G**) and TMR-HALO-FGFR3 MFIs were used to calculate ratios of surface (**H**) and internal (**I**) FGFR3 levels in cells stimulated with FGF-8b for 30 min versus unstimulated cells. Ratios were calculated based on the data displayed in Supplementary Fig. S3B. Histograms in (**G**) show 1 representative replica of data quantified in (**H**, **I**), which are represented as mean ± SD of *HALO-Fgfr3^{FL}*, *HALO-Fgfr3^{FL}-K502R*, *HALO-Fgfr3$^{\Delta E18}$*, *HALO-Fgfr3^{FL}-Tacc3*, *HALO-Fgfr3$^{\Delta E18}$-Tacc3*, FGF-8b, 0 min, 30 min, *n*=4; *Fgfr3$^{\Delta E18}$-K502R-Tacc3*, *n*=3 independent replica. *P* values in (**E, H, I**) were calculated with ordinary one-way ANOVA and FDR multiple testing corrections.

revealed a high prevalence of adenocarcinomas, papillary carcinomas and mesotheliomas, in contrast to the mainly healthy tissue or low-grade adenoma lesions observed in lungs of the other *Fgfr3* cohorts (Supplementary Fig. S4B). The transforming capacity of *Fgfr3$^{\Delta E18}$-Tacc3-P2A-Cre* was markedly exacerbated when lungs of *Trp53$^{F/F}$* animals were intubated (**Fig. 5C**), with >90% of lungs presenting high-grade lesions including mesotheliomas and mixed mesothelioma and adenocarcinoma histotypes (Supplementary Fig. S4B). In contrast, expression of *Fgfr3^{FL}-P2A-Cre*, *Fgfr3$^{\Delta E18}$-P2A-Cre* or *Fgfr3^{FL}-Tacc3-P2A-Cre* in the lungs of *Trp53$^{F/F}$* mice only marginally increased tumor formation as compared to *Cre*-injected animals (**Fig. 5C**; Supplementary Fig. S4B). In sum, in both wild-type and *Trp53$^{F/F}$* mice, only the *Fgfr3$^{\Delta E18}$-Tacc3* fusion had the competence to effectively drive lung tumorigenesis.

Apart from lung cancers, *FGFR3$^{\Delta E18}$-TACC3* fusions have also been reported in cancers of the breast [23–25]. We identified 25 breast cancer cases harboring *FGFR3$^{\Delta E18}$-TACC3* REs in the FMI cohort (**Fig. 1A**; Supplementary Data S1) and 3 cases in the HMF cohort (**Fig. 1D** and **2B**; Supplementary Data S2). In the context of breast cancer, FGFR3-TACC3 fusions have been assessed *in vitro* [23,24], yet, to our best knowledge, no *in vivo* studies have been conducted. We evaluated the oncogenicity of *Fgfr3* variants in mouse mammary tumor models representing different breast cancer subtypes, including invasive lobular carcinoma (ILC) that is characterized by the loss of E-cadherin, which is encoded by *CDH1* [34,35].

A

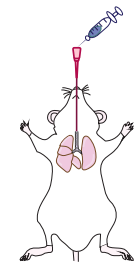

Intratracheal lentiviral injections

B

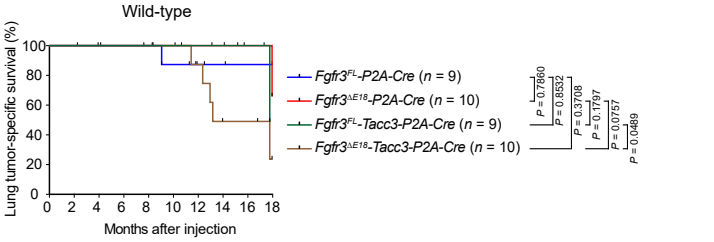

C

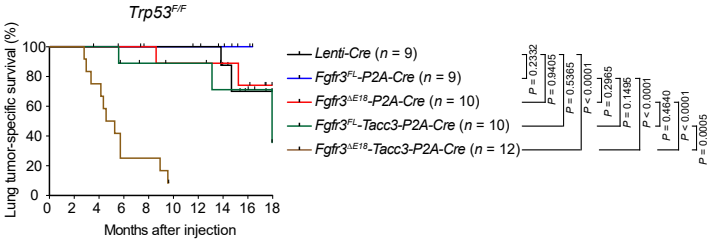

D

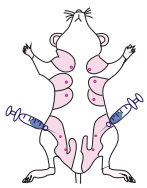

Intraductal lentiviral injections

E

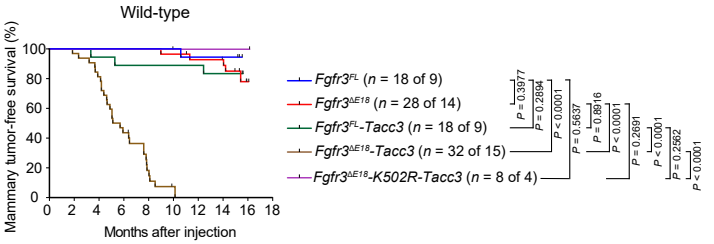

F

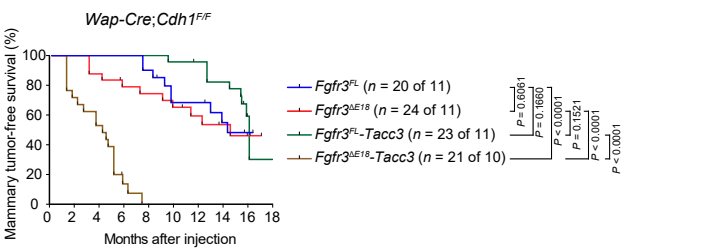

Figure 5. *Fgfr3$^{\Delta E18}$-Tacc3* fusions drive mouse lung and mammary tumorigenesis.

A, Overview of the somatic mouse model for lung cancer formation consisting of intratracheal intubation and delivery of lentiviral vectors encoding the *Fgfr3* variants of interest. **B,** Kaplan-Meier curves showing lung tumor-specific survival of female wild-type mice administered with lentiviruses encoding the indicated *Fgfr3* variants via intratracheal intubation. *Fgfr3^{FL}-P2A-Cre*, *n*=9; *Fgfr3$^{\Delta E18}$-P2A-Cre*, *n*=10; *Fgfr3^{FL}-Tacc3 -P2A-Cre*, *n*=9; *Fgfr3$^{\Delta E18}$-Tacc3-P2A-Cre*, *n*=10 mice. **C,** Kaplan-Meier curves showing lung tumor-specific survival of female *Trp53$^{F/F}$* mice administered with lentiviruses encoding the indicated *Fgfr3* variants via intratracheal intubation. *Lenti-Cre* control, *n*=9; *Fgfr3^{FL}-P2A-Cre*, *n*=9; *Fgfr3$^{\Delta E18}$-P2A-Cre*, *n*=10; *Fgfr3^{FL}-Tacc3 -P2A-Cre*, *n*=10; *Fgfr3$^{\Delta E18}$-Tacc3 -P2A-Cre*, *n*=12 mice. **D,** Overview of the somatic mouse model for mammary gland-specific overexpression of indicated *Fgfr3* variants via intraductal injection of lentiviruses. Two glands per mouse were injected. **E,** Kaplan-Meier curves showing mammary tumor-free survival of female wild-type mice intraductally injected with lentiviruses encoding indicated *Fgfr3* variants. *Fgfr3^{FL}*, *n*=18 of 9; *Fgfr3$^{\Delta E18}$*, *n*=28 of 14; *Fgfr3^{FL}-Tacc3*, *n*=18 of 9; *Fgfr3$^{\Delta E18}$-Tacc3*, *n*=32 of 15; *Fgfr3$^{\Delta E18}$-K502R-Tacc3*, *n*=8 injected mammary glands of 4 mice. **F,** Kaplan-Meier curves showing mammary tumor-free survival of female *Wap-Cre;Cdh1$^{F/F}$* mice intraductally injected with lentiviruses encoding indicated *Fgfr3* variants. *Fgfr3^{FL}*, *n*=20 of 11; *Fgfr3$^{\Delta E18}$*, *n*=24 of 11; *Fgfr3^{FL}-Tacc3*, *n*=23 of 11; *Fgfr3$^{\Delta E18}$-Tacc3*, *n*=21 injected mammary glands of 10 mice. *P* values were calculated with log-rank (Mantel-Cox) tests (**B, C, E, F**).

Using intraductal injections (**Fig. 5D**; refs. [5,36]), we somatically delivered lentiviruses containing *Fgfr3* variants to the mammary glands of female wild-type (**Fig. 5E**; Supplementary Fig. S5A) and *Wap-Cre;Cdh1$^{F/F}$* (**Fig. 5F**; Supplementary Fig. S5B) mice. Mammary glands injected with *Fgfr3^{FL}*, *Fgfr3$^{\Delta E18}$*, *Fgfr3^{FL}-Tacc3* or *Fgfr3$^{\Delta E18}$-K502R-Tacc3* variants displayed no (**Fig. 5E**) or slow (**Fig. 5F**) tumorigenesis, whereas those injected with the *Fgfr3$^{\Delta E18}$-Tacc3* fusion showed marked tumor formation in both genotypes (**Fig. 5E** and **F**). Reminiscent of the histopathological observations in lung, mammary glands of wild-type mice injected with *Fgfr3^{FL}*, *Fgfr3$^{\Delta E18}$* and *Fgfr3^{FL}-Tacc3* variants revealed mostly no or low-grade lesions, whereas glands injected with *Fgfr3$^{\Delta E18}$-Tacc3* contained high-grade tumors, such as adenocarcinomas and squamous metaplastic carcinomas (Supplementary Fig. S5C). Similarly, mammary glands of *Wap-Cre;Cdh1$^{F/F}$* mice injected with *Fgfr3^{FL}*, *Fgfr3$^{\Delta E18}$* and *Fgfr3^{FL}-Tacc3* variants mostly revealed healthy tissue, low-grade lesions, or classic ILCs. Notably, the low-grade lesions and classic ILCs observed in the *Wap-Cre;Cdh1$^{F/F}$* cohorts likely represent spontaneous tumor events owing to the ILC-predisposition of this strain [5,37]. In contrast, mammary glands injected with *Fgfr3$^{\Delta E18}$-Tacc3* displayed tumors of higher grade, especially solid ILCs (Supplementary Fig. S5C).

Together, our *in vivo* modeling efforts uncovered that the *Fgfr3$^{\Delta E18}$-Tacc3* fusion is a potent driver in mouse models of both lung and breast tumorigenesis, whereas the loss of the C-terminal tail of FGFR3 on its own was insufficient to induce tumor formation. Finally, we explored driver gene alterations diagnosed by FMI's oncogenomic profiling and their incidence in cancers with *FGFR3$^{\Delta E18}$* alterations. Tumors that harbored *FGFR3* E18 truncations devoid of a partner gene (i.e., E18-truncating mutations, intergenic or internal REs, or partial amplifications) showed enrichment for alterations in *KRAS*, *ERBB2*, *MYC*, *PIK3CA*, and *PTEN*, as compared to tumors that contained a *FGFR3$^{\Delta E18}$* RE/fusion with a partner gene (Supplementary Fig. S4A and S5D-S5G), suggesting that additional tumor drivers may be required to enable oncogenicity of *FGFR3$^{\Delta E18}$* alterations without a partner gene.

Self-interacting capacity but not mitotic function of TACC3 is required for FGFR3$^{\Delta E18}$-TACC3 oncogenicity

The high prevalence of self-interacting domains among all FGFR3 fusion partners (**Fig. 3B-D**) and the preservation of the two TACC3-CC domains in most of the FGFR3$^{\Delta E18}$-TACC3 fusions (**Fig. 3E** and **F**), suggested that the presence of a self-interacting domain is a prerequisite for the oncogenic activity of FGFR3$^{\Delta E18}$. To assess the relevance of the TACC3-CC domains for the oncogenic competence of FGFR3$^{\Delta E18}$-TACC3, we substituted key AA residues critical for the integrity of either of the two CC domains, as identified by the Paircoil2 algorithm [38], with prolines (**Fig. 6A**; Supplementary Methods S2 and S3). Intraductal injection of *Fgfr3$^{\Delta E18}$-Tacc3$^{CC1\text{-}Pro}$* or *Fgfr3$^{\Delta E18}$-Tacc3$^{CC2\text{-}Pro}$* variants that encode FGFR3$^{\Delta E18}$-TACC3 derivatives predicted to lack dimerization capacity, did not induce tumor formation in wild-type mice, in contrast to parental FGFR3$^{\Delta E18}$-TACC3 that retains dimerization and drives marked tumorigenesis (**Fig. 6B**; Supplementary Fig. S5H). These findings underscored the requirement of functional TACC3-CC domains for full oncogenic capacity of FGFR3$^{\Delta E18}$-TACC3.

TACC3 facilitates centrosome-dependent microtubule assembly [39], mediates kinetochore-microtubule attachment [40], and ensures spindle-dependent chromosome alignment [41–43] throughout mitosis. These functions require phosphorylation of TACC3 at S558 by Aurora-kinase A (AURKA), followed by binding of clathrin at L566/L567 [39,44–48]. Both the AURKA phosphorylation site as well as the clathrin binding site are located to a structural unit that is encoded by E8 of human *TACC3* and are retained in the clinical *FGFR3$^{\Delta E18}$-TACC3$^{E8\text{-}E16}$* fusion and in the corresponding murine *Fgfr3$^{\Delta E18}$-Tacc3* used in this study. To test whether the two TACC3 regulatory sites are critical for FGFR3$^{\Delta E18}$-TACC3 oncogenicity, we generated the *Fgfr3$^{\Delta E18}$-Tacc3^{S764A}* and the *Fgfr3$^{\Delta E18}$-Tacc3$^{L772A/L773A}$* variants with mutated AURKA phosphorylation or clathrin binding sites, respectively (**Fig. 6A**; Supplementary Methods S4 and S5). We also generated the *Fgfr3$^{\Delta E18}$-Tacc3$^{E10\text{-}E16}$* variant that corresponds to the human *FGFR3$^{\Delta E18}$-TACC3$^{E11\text{-}E16}$* fusion recurrently observed in clinical samples (**Fig. 3E** and **F**) and that lacks both the AURKA phosphorylation and the clathrin binding sites in TACC3 (**Fig. 6A**; Supplementary Methods S6). Intraductal injection of the *Fgfr3$^{\Delta E18}$-Tacc3$^{E10\text{-}E16}$* fusion into wild-type mice modestly increased tumor latency as compared to the *Fgfr3$^{\Delta E18}$-Tacc3* cohort, and similarly to that of *Fgfr3$^{\Delta E18}$-Tacc3^{S764A}* and the *Fgfr3$^{\Delta E18}$-Tacc3$^{L772A/L773A}$* (**Fig. 6C**). However, there was no statistically significant difference in the overall survival among the four mouse cohorts (Supplementary Fig. S5I), suggesting that the assessed TACC3-regulatory sites are negligible for the oncogenicity of the FGFR3$^{\Delta E18}$-TACC3 fusion, in agreement with previous *in vitro* work [49].

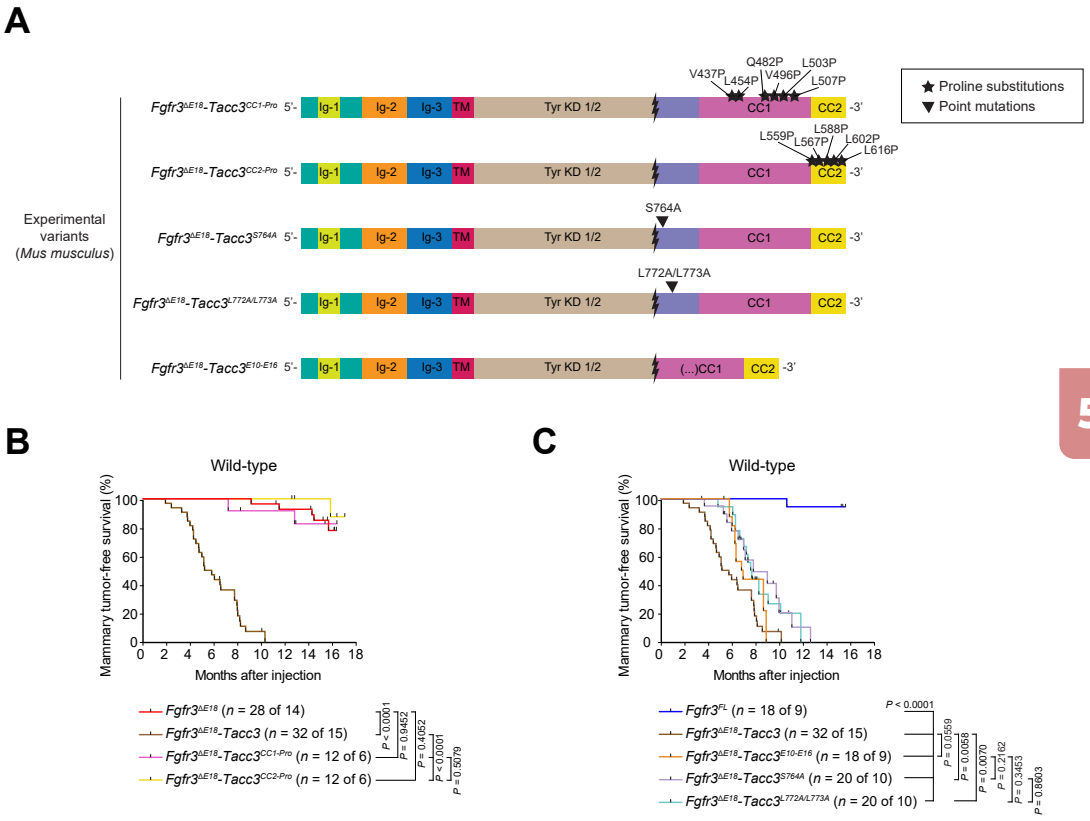

Figure 6. Self-interacting capacity but not mitotic function of TACC3 is required for oncogenicity of the FGFR3$^{\Delta E18}$-TACC3 fusion.

A, Schematic representation of the protein structure of the cloned mouse variants *Fgfr3*$^{\Delta E18}$-*Tacc3*$^{CC1\text{-}Pro}$ and *Fgfr3*$^{\Delta E18}$-*Tacc3*$^{CC2\text{-}Pro}$ (disrupted CC domain mutants), *Fgfr3*$^{\Delta E18}$-*Tacc3*^{S764A} (abrogated AURKA phosphorylation site mutant), *Fgfr3*$^{\Delta E18}$-*Tacc3*$^{L772A/L773A}$ (suppressed clathrin binding site mutant), and *Fgfr3*$^{\Delta E18}$-*Tacc3*$^{E10\text{-}E16}$. The Paircoil2 algorithm [38] was used to detect the two main CC motifs in the TACC3 protein sequence and to predict the likelihood of their abrogation by substituting key leucine (L), valine (V), and/or glutamine (Q) AA residues by prolines (P). Exact point mutations and proline substitutions are indicated. Complete nucleotide and AA changes are disclosed in Supplementary Methods S2-S6. **B, C,** Kaplan-Meier curves showing mammary tumor-free survival of female wild-type mice intraductally injected with lentiviruses encoding indicated *Fgfr3* variants. *Fgfr3*$^{\Delta E18}$, *n*=28 of 14; *Fgfr3*$^{\Delta E18}$-*Tacc3*, *n*=32 of 15; *Fgfr3*$^{\Delta E18}$-*Tacc3*$^{CC1\text{-}Pro}$, *n*=12 of 6; *Fgfr3*$^{\Delta E18}$-*Tacc3*$^{CC2\text{-}Pro}$, *n*=12 of 6; *Fgfr3*^{FL}, *n*=18 of 9; *Fgfr3*$^{\Delta E18}$-*Tacc3*$^{E10\text{-}E16}$, *n*=18 of 9; *Fgfr3*$^{\Delta E18}$-*Tacc3*^{S764A}, *n*=20 of 10; *Fgfr3*$^{\Delta E18}$-*Tacc3*$^{L772A/L773A}$, *n*=20 injected mammary glands of 10 mice. The *Fgfr3*$^{\Delta E18}$ curve in **(B)**, the *Fgfr3*^{FL} curve (**C**), and the *Fgfr3*$^{\Delta E18}$-*Tacc3* curves in (**B, C**) are duplicated from (**Fig. 5E**). *P* values were calculated with log-rank (Mantel-Cox) tests.

Oncogenicity of *Fgfr3$^{\Delta E18}$-Add1*, *Fgfr3$^{\Delta E18}$-Tnip2*, and *Fgfr3$^{\Delta E18}$-Jakmip1* fusions

To assess whether FGFR3$^{\Delta E18}$ fusions other than FGFR3$^{\Delta E18}$-TACC3 had oncogenic capacity, we functionally assessed three previously uncharacterized *FGFR3* fusions identified in the FMI and HMF cohorts (**Fig. 1A**, **1D**, **2C**, **3A** and **3B**; Supplementary Data S1 and S2). These were *FGFR3$^{\Delta E18}$-ADD1$^{E3\text{-}E15}$* (6 cases), *FGFR3$^{\Delta E18}$-TNIP2$^{E2\text{-}E6}$* (11 cases), and *FGFR3$^{\Delta E18}$-JAKMIP1$^{E4\text{-}E13}$* (4 cases; **Fig. 7A**). Notably, all three fusion proteins contained self-dimerizing domains from ADD1, TNIP2 and JAKMIP1, respectively (**Fig. 3B** and **7A**).

Stable expression of the murine orthologs *Fgfr3$^{\Delta E18}$-Add1*, *Fgfr3$^{\Delta E18}$-Tnip2*, and *Fgfr3$^{\Delta E18}$-Jakmip1* in NMuMG cells (Supplementary Fig. S2A and S6A) led to activation of downstream FGFR3 signaling under serum-deprived conditions, which was abrogated by treatment with fexagratinib (**Fig. 7B**; Supplementary Fig. S6A). Similar to *Fgfr3$^{\Delta E18}$-Tacc3* and hotspot mutant *Fgfr3^{K644E}* (corresponding to human *FGFR3^{K650E}*; ref. [49]), all three fusions triggered robust phosphorylation of FGFR3, EIF4EBP1, ERK1/2 and FRS2, consistent with activation of FGFR, mTOR, and MAPK signaling. *Fgfr3$^{\Delta E18}$-Add1* additionally induced strong phosphorylation of RPS6, STAT1, and STAT3, resembling levels of *Fgfr3$^{\Delta E18}$-Tacc3*.

FGFR3 fusions involving *ADD1*, *TNIP2* and *JAKMIP1* were predominantly identified in urothelial cancer (**Fig. 1A** and **1D**; Supplementary Data S1 and S2). Therefore, we made use of the human bladder cancer 5637 cell line that harbors an activating *ERBB2^{S310F}* mutation and EGFR overexpression and is sensitive to the dual ERBB2/EGFR tyrosine kinase inhibitors (TKIs) afatinib and dacomitinib (**Fig. 7C** and **7D**; Supplementary Fig. S6B-S6E). Expression of *Fgfr3$^{\Delta E18}$-Tacc3*, *Fgfr3$^{\Delta E18}$-Add1*, *Fgfr3$^{\Delta E18}$-Tnip2*, *Fgfr3$^{\Delta E18}$-Jakmip1*, as well as *Fgfr3^{K644E}* conferred marked resistance to both TKIs, and sensitivity to afatinib was restored when cells were co-treated with the FGFRi fexagratinib (**Fig. 7C-F**; Supplementary Fig. S6D-S6G).

Figure 7. *In vitro* activity and *in vivo* tumorigenicity of *Fgfr3$^{\Delta E18}$-Add1*, *Fgfr3$^{\Delta E18}$-Tnip2* and *Fgfr3$^{\Delta E18}$-Jakmip1* gene fusions.

A, Schematic representation of the FGFR3$^{\Delta E18}$-ADD1, FGFR3$^{\Delta E18}$-TNIP2 and FGFR3$^{\Delta E18}$-JAKMIP1 fusions detected in the FMI and HMF cohorts. Complete nucleotide and AA sequences for the corresponding murine experimental constructs used are disclosed in Supplementary Methods S7-S9. **B,** Quantifications of indicated phosphoprotein band intensities based on Western blots in Supplementary Fig. S6A, where 24 hr serum-starved NMuMG cells stably expressing *GFP*, *Fgfr3^{FL}*, *Fgfr3$^{\Delta E18}$*, *Fgfr3^{FL}-Tacc3*, *Fgfr3$^{\Delta E18}$-Tacc3*, *Fgfr3$^{\Delta E18}$-Add1*, *Fgfr3$^{\Delta E18}$-Tnip2*, *Fgfr3$^{\Delta E18}$-Jakmip1*, or *Fgfr3^{K644E}* were treated for 3 hr with either vehicle or 1 μM fexagratinib. Phospho band intensities were normalized to their individual lane backgrounds and to their corresponding total protein band intensities and β-actin bands, and unit variance scaling is applied to the rows. **C,** Dose-response curves of 5637 bladder cancer cells, either untransduced (parental) or stably expressing the indicated *Fgfr3* variants via lentiviral transduction, treated for 3 days with different concentrations of afatinib. Cell viability was determined using CellTiter-Blue. Data were normalized to untreated conditions within each cell line and are presented as mean ± SD of *n*=2 independent replica from 1 representative experiment. Assays were performed at least 2 independent times. **D,** Representative well images of (**C**), obtained after fixing and staining the cells with crystal violet. **E,** Dose-response curves of 5637 bladder cancer cells as in (**C**), treated for 3 days with different concentrations of afatinib in combination with 2.5 μM fexagratinib, corresponding to the inhibitory concentration (IC)10-IC20. **F,** Representative well images of (**E**). **G,** Kaplan-Meier curves showing mammary tumor-free survival of female wild-type mice intraductally injected with lentiviruses encoding indicated *Fgfr3* variants. *Fgfr3$^{\Delta E18}$*, *n*=28 of 14; *Fgfr3$^{\Delta E18}$-Tacc3*, *n*=32 of 15; *Fgfr3$^{\Delta E18}$-Add1*, *n*=28 of 14; *Fgfr3$^{\Delta E18}$-Tnip2*, *n*=28 of 14; *Fgfr3$^{\Delta E18}$-Jakmip1*, *n*=24 injected mammary glands of 12 mice. The *Fgfr3$^{\Delta E18}$* and the *Fgfr3$^{\Delta E18}$-Tacc3* curves are duplicated from (**Fig. 5E**). *P* values were calculated with log-rank (Mantel-Cox) tests.

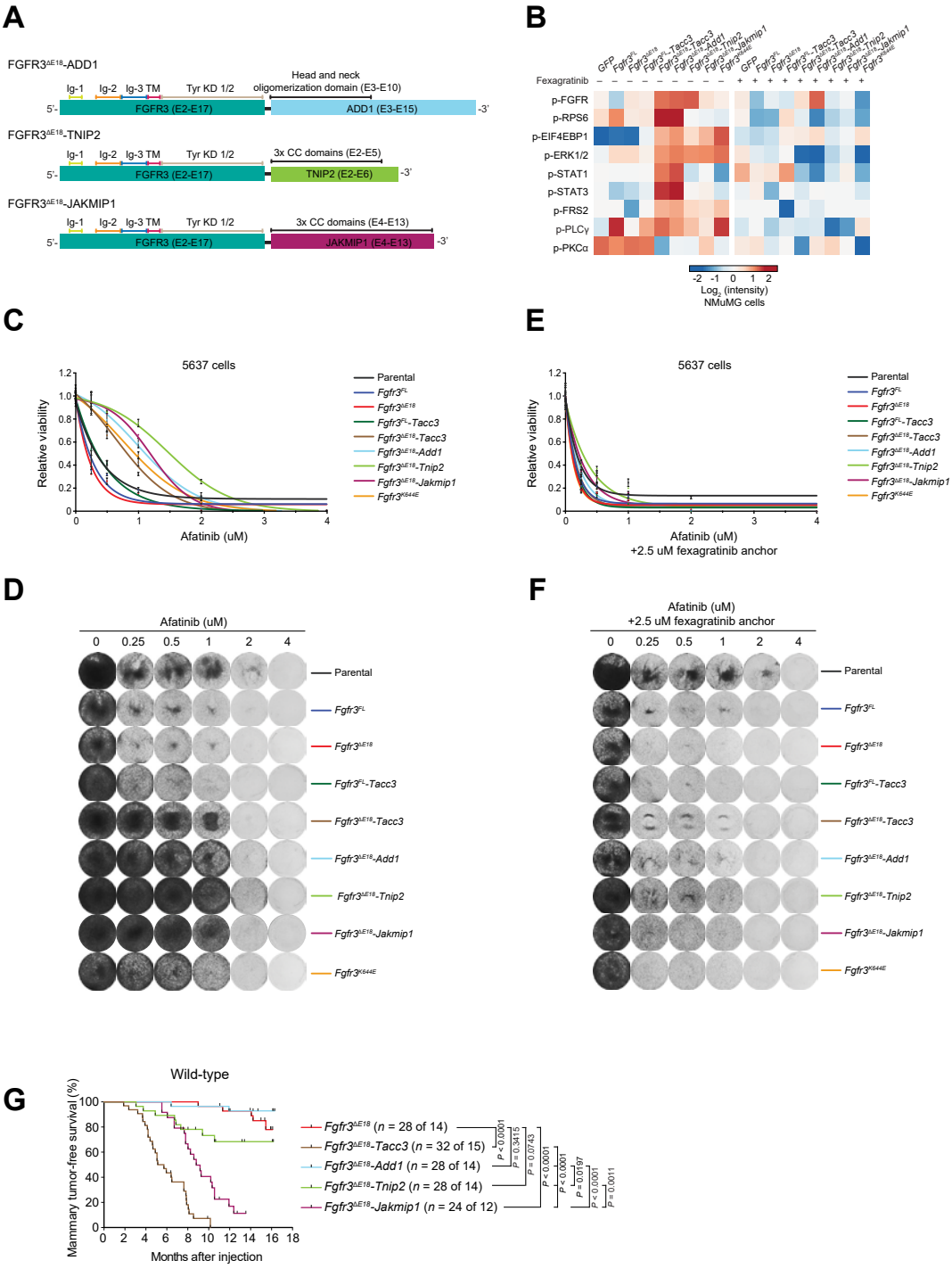
A
FGFR3ΔE18-ADD1
Ig-1
Ig-2
Ig-3 TM
Tyr KD 1/2
Head and neck oligomerization domain (E3-E10)
5'-
FGFR3 (E2-E17)
ADD1 (E3-E15)
-3'
FGFR3ΔE18-TNIP2
3x CC domains (E2-E5)
TNIP2 (E2-E6)
FGFR3ΔE18-JAKMIP1
3x CC domains (E4-E13)
JAKMIP1 (E4-E13)
B
GFP
Fgfr3FL
Fgfr3ΔE18
Fgfr3FL-Tacc3
Fgfr3ΔE18-Tacc3
Fgfr3ΔE18-Add1
Fgfr3ΔE18-Tnip2
Fgfr3ΔE18-Jakmip1
Fgfr3K644E
Fexagratinib
p-FGFR
p-RPS6
p-EIF4EBP1
p-ERK1/2
p-STAT1
p-STAT3
p-FRS2
p-PLCγ
p-PKCα
Log2 (intensity)
NMuMG cells
C
5637 cells
Relative viability
Afatinib (uM)
Parental
Fgfr3FL
Fgfr3ΔE18
Fgfr3FL-Tacc3
Fgfr3ΔE18-Tacc3
Fgfr3ΔE18-Add1
Fgfr3ΔE18-Tnip2
Fgfr3ΔE18-Jakmip1
Fgfr3K644E
E
5637 cells
Relative viability
Afatinib (uM)
+2.5 uM fexagratinib anchor
D
Afatinib (uM)
0
0.25
0.5
1
2
4
F
Afatinib (uM)
+2.5 uM fexagratinib anchor
G
Wild-type
Mammary tumor-free survival (%)
Months after injection
Fgfr3ΔE18 (n = 28 of 14)
Fgfr3ΔE18-Tacc3 (n = 32 of 15)
Fgfr3ΔE18-Add1 (n = 28 of 14)
Fgfr3ΔE18-Tnip2 (n = 28 of 14)
Fgfr3ΔE18-Jakmip1 (n = 24 of 12)
P < 0.0001
P = 0.3415
P = 0.0743
P < 0.0001
P < 0.0001
P = 0.0197
P < 0.0001
P = 0.0011

Intraductal injection of *Fgfr3$^{\Delta E18}$-Add1*, *Fgfr3$^{\Delta E18}$-Tnip2* and *Fgfr3$^{\Delta E18}$-Jakmip1* fusions into the mammary glands of wild-type mice revealed that *Fgfr3$^{\Delta E18}$-Jakmip1* robustly induced mammary tumorigenesis, comparable to *Fgfr3$^{\Delta E18}$-Tacc3* (**Fig. 7G**; Supplementary Fig. S6H). In contrast, *Fgfr3$^{\Delta E18}$-Tnip2* induced tumors in only a fraction of the injected mammary glands and *Fgfr3$^{\Delta E18}$-Add1* completely failed to induce mammary tumorigenesis despite displaying considerable activity *in vitro* (**Fig. 7B-D** and **7G**; Supplementary Fig. S6). These differences in *in vivo* oncogenicity in wild-type mouse mammary epithelium suggest that the oncogenic competence of FGFR3 fusions may be affected by the mutational context as well as the tissue of origin – *ADD1* fusions were mostly found in urothelial cancer. In sum, our results extend the tumor- and drug resistance-driving properties of FGFR3$^{\Delta E18}$ fusions beyond TACC3, underscoring the potential of FGFR-targeted therapies in these settings.

Fgfr3$^{\Delta E18}$-Tacc3-driven mammary tumors are sensitive to FGFRi

Finally, we tested whether mammary tumors driven by *Fgfr3$^{\Delta E18}$-Tacc3* would be sensitive to FGFR-targeted therapy, by orthotopically transplanting tumor pieces into the mammary fat pad of syngeneic recipient female mice. When tumors reached a size of 62.5 mm^3, animals were subjected to an intermittent dosing regimen using 12.5 mg/kg/day of fexagratinib (**Fig. 8A**; refs. [26,50]). Fexagratinib treatment in mice engrafted with *Fgfr3$^{\Delta E18}$-Tacc3*-induced tumors derived from either wild-type (**Fig. 8B**; Supplementary Fig. S7A) or *Wap-Cre;Cdh1$^{F/F}$* (**Fig. 8C**; Supplementary Fig. S7B) donors was efficacious by significantly suppressing tumor growth as compared to the respective vehicle-treated controls, although complete tumor regression was not achieved. We next subjected tumor-bearing mice to a PK/PD study using a daily 12.5 mg/kg dose of fexagratinib for 2 or 5 consecutive days. Analysis of plasma and tumor samples 1 hr post dosing confirmed high fexagratinib exposure, with plasma and intratumoral concentrations reaching several orders of magnitude above the reported *in vitro* IC50 of ~1.8 nmol/L for FGFR3 (Supplementary Fig. S7C-S7E; ref. [26]), ruling out insufficient drug exposure as a limiting factor in the efficacy study. PD biomarker assessment demonstrated substantial on-target FGFR3 inhibition as well as FGFR3 signaling pathway suppression (Supplementary Fig. S7F and S7G), confirming that the dosing regimen achieved effective target engagement. To further investigate the lack of complete tumor eradication upon fexagratinib treatment, we analyzed protein lysates from endpoint tumors in both wild-type and *Wap-Cre;Cdh1$^{F/F}$* donors that had progressed during fexagratinib treatment (Supplementary Fig. S7H-S7K). Western blot analysis revealed reactivation of FGFR3 downstream signaling in a fraction of the fexagratinib-treated tumors. Notably, the remaining tumors did not show pathway reactivation during treatment outgrowth, suggesting that resistance may also arise through FGFR3 signaling-independent mechanisms, such as tumor cell plasticity or stromal changes including the immune compartment [4,50,51]. Nonetheless, our data demonstrated that tumors driven by the *Fgfr3$^{\Delta E18}$-Tacc3* oncogene are sensitive to FGFRi, thus validating the use of FGFR-targeted therapy for FGFR3$^{\Delta E18}$-TACC3 fusion-positive cancers.

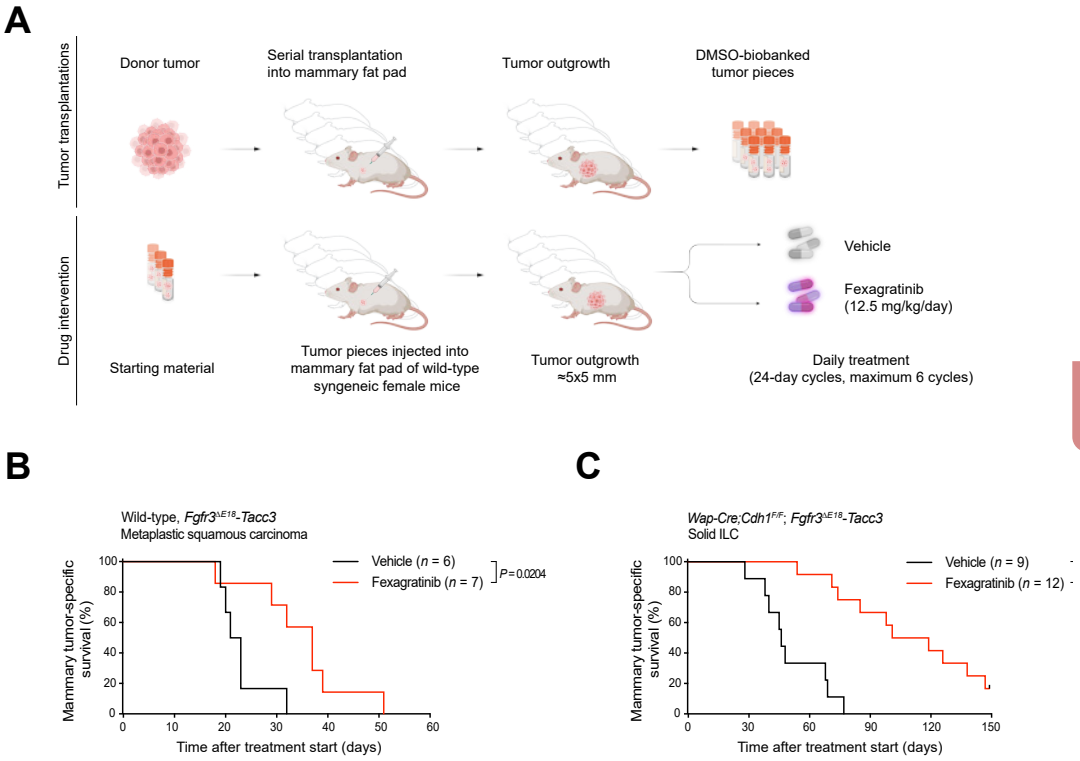

Figure 8. *Fgfr3*$^{\Delta E18}$*-Tacc3*-driven mammary tumors are sensitive to FGFRi.

A, Schematic overview of the mammary tumor transplantation setup and subsequent FGFRi intervention study fexagratinib (partially created with BioRender.com). **B, C,** Kaplan-Meier curves showing mammary tumor-specific survival of female syngeneic wild-type (**B**) or *Wap-Cre;Cdh1*$^{F/F}$ (**C**) mice bearing mammary fat pad transplants derived from indicated tumor donors and treated daily orally with vehicle or 12.5 mg/kg fexagratinib using an intermittent dosing regimen [50]. *P* values were calculated with log-rank (Mantel-Cox) tests.

DISCUSSION

Our previous work uncovered E18-truncated *FGFR2* to be a potent driver alteration in cancer that is highly sensitive to FGFR2-targeting [5]. This finding has substantially broadened the spectrum of cancer patients who benefit from FGFR-targeted therapies [5,6]. Here we set out to elucidate the landscape of E18-truncating *FGFR3* alterations in cancer to understand whether our previous findings in *FGFR2* translate to its paralog *FGFR3*. In-depth oncogenomic analyses of *FGFR3* REs enabled the comprehensive detection of alterations that likely promote the expression of *FGFR3*$^{\Delta E18}$, either by *FGFR3* E18-truncating mutations or structural REs. Although many *FGFR3* REs were initially classified as having an unknown

reading frame at the DNA level, analysis of matched RNA-seq data showed that most of these events produce in-frame RE transcripts (**Fig. 1D** and **2B**). The predominance of self-interacting domains in the FGFR3$^{\Delta E18}$ RE partners (**Fig. 3B** and **C**), indicated that a RE partner with a conserved self-interacting domain might be a prerequisite for the oncogenic activity of FGFR3$^{\Delta E18}$. Among structural REs resulting in *FGFR3*$^{\Delta E18}$, *TACC3* emerged as the most frequent RE partner (85%), with most cases conserving its two CC domains intact as part of the fusion (**Fig. 3**). *FGFR3-TACC3* fusions have been identified in multiple solid tumor types, particularly in glioblastoma, urothelial, lung and breast cancers [8,11,13,23,24], consistent with our own analyses (**Fig. 1A** and **D**).

Notably, 12.3% of all *FGFR3* alterations were E18-truncating mutations potentially producing C-terminally truncated FGFR3 devoid of any fusion partner (**Fig. 1A**). In the case of *FGFR2*, the oncogenic competence of different alteration types depends on distinct co-occurring driver mutations. For instance, *FGFR2* hotspot mutations and *FGFR2*$^{\Delta E18}$ alterations cooperate with *PIK3CA* hotspot mutations to drive PI3K signaling [5,52]. Conversely, *FGFR2* amplifications co-occur with *TP53* mutations, *PTEN* loss-of-function, and *MYC*, *CCND1*, and *FGF3/4/19* amplification [5,53,54], and FGFR2 functionally cooperates with these driver alterations to promote tumorigenesis [5]. The oncogenic competence of *FGFR3* E18-truncating mutations and *FGFR3* REs devoid of a partner gene might likewise depend on cooperation with specific co-drivers, as suggested by the co-occurrence of *KRAS*, *ERBB2*, *MYC*, *PIK3CA*, and *PTEN* alterations in this subset of *FGFR3* alterations (Supplementary Fig. S5D-S5G).

We set out to model identified *FGFR3* alterations in disease-relevant animal models; however, somatic gene delivery to tissues of the urothelial tract has remained technically challenging due to a resistant urothelial barrier and the lack of efficient delivery methods. We therefore focused our efforts on testing the *in vivo* oncogenicity of *Fgfr3* variants in lung and mammary gland tumorigenesis. We demonstrated a causal role of FGFR3$^{\Delta E18}$-TACC3 fusions in tumor formation in both settings (**Fig. 5**; Supplementary Fig. S4B and S5A-S5C). The oncogenic capacity of *FGFR3-TACC3* fusions has been previously addressed in glioblastoma and lung tumor formation *in vivo* [13,18]. This is in line with our own results for lung tumorigenesis, where we employed additional controls to confirm that both the loss of the C-terminal tail of FGFR3 (FGFR3$^{\Delta E18}$) as well as the fusion of a dimerization domain-containing TACC3 portion are required for complete tumor driving potential (**Fig. 5A-C**; Supplementary Fig. S4B). Our data showed that the oncogenic capacity of FGFR3$^{\Delta E18}$-TACC3 is fully dependent on intact CC domains of TACC3, since CC disruption by key proline substitutions hindered FGFR3$^{\Delta E18}$-TACC3 oncogenicity (**Fig. 6A** and **B**; Supplementary Fig. S5H). These findings are supported by previous *in vitro* work suggesting considerable relevance of the TACC3 CC domains for cell transformation and aberrant downstream signaling induction by FGFR3-TACC3 fusions [30,55]. Moreover, the majority of the *FGFR3* fusions found in cancer involve partner genes with retained expression of a dimerization

domain, which can facilitate ligand-independent receptor dimerization and signaling [5,56].

In this study, we characterized three additional, previously untested *FGFR3*$^{\Delta E18}$ fusions: *FGFR3*$^{\Delta E18}$*-ADD1*, *FGFR3*$^{\Delta E18}$*-TNIP2*, and *FGFR3*$^{\Delta E18}$*-JAKMIP1*. All three variants activated downstream FGFR3 signaling in a kinase-dependent manner and conferred resistance to ERBB2/EGFR TKIs *in vitro*, yet remained sensitive to FGFRi (**Fig. 7**; Supplementary Fig. S6), underscoring a therapeutic opportunity in clinical settings. Intriguingly, the *in vivo* oncogenicity of these fusions in wild-type mouse mammary epithelium diverged: *Fgfr3*$^{\Delta E18}$*-Jakmip1* acted as a *bona fide* tumor driver, whereas *Fgfr3*$^{\Delta E18}$*-Tnip2* displayed an intermediate phenotype, and *Fgfr3*$^{\Delta E18}$*-Add1* failed to induce tumors (**Fig. 7G**; Supplementary Fig. S6H). These differences suggest that *in vivo* tumorigenicity of *FGFR3*$^{\Delta E18}$ fusions may be dependent on the target tissue, as *FGFR3*$^{\Delta E18}$*-ADD1* and *FGFR3*$^{\Delta E18}$*-TNIP2* fusions are prevalent in urothelial cancer rather than breast cancer. Additionally, these fusions might require specific genomic co-alterations to achieve full oncogenic competence, as proposed for *FGFR3*$^{\Delta E18}$ alterations without a fusion partner. Moreover, ADD1 contains a dimerizing head-and-neck domain, as opposed to the CC domains in TACC3, TNIP2, and JAKMIP1 (**Fig. 7A**). These different structural features might impact *in vivo* dimerization capacity of FGFR3$^{\Delta E18}$-ADD1 and ultimately oncogenicity.

Previous research has suggested that the contribution of TACC3 to the oncogenic potential of FGFR3$^{\Delta E18}$-TACC3 fusions might extend beyond merely providing a self-interacting domain. Singh *et al*. [13] proposed that the FGFR3-TACC3 fusion locates to the mitotic spindle poles via the retained CC domain, leading to chromosomal segregation defects, aneuploidy, and eventually oncogenic transformation. However, others [57] have not observed direct localization of the fusion protein at the mitotic spindle and attribute the observed mitotic defects to the fusion's CC domain-mediated sequestration of endogenous TACC3 from the mitotic spindle. Our results show that the physiological role of TACC3 in mitotic spindle assembly and microtubule stability is dispensable for the oncogenic potential of the FGFR3$^{\Delta E18}$-TACC3 fusion (**Fig. 6C**; Supplementary Fig. S5I). Additionally, while impaired internalization of the FGFR3$^{\Delta E18}$-TACC3 fusion upon ligand stimulation may contribute to sustained kinase signaling, it is not the primary driver of its oncogenicity. Both FGFR3$^{\Delta E18}$ and FGFR3$^{\Delta E18}$-TACC3 lack the C-terminal tail that contains the YXXΦ endocytosis internalization motif and accordingly show impaired receptor internalization (**Fig. 4G-I**), yet only the fusion variant is capable of inducing tumor formation (**Fig. 5**) and *in vitro* transformation (**Fig. 4B-F**; Supplementary Fig. S2B-S2E). This indicates that receptor accumulation at the cell membrane alone is insufficient to promote oncogenic signaling.

We recently identified a conserved C-terminal phenylalanine-serine motif in FGFR2 that mediates binding of the C-terminal tail to the kinase domain and suppresses RTK signaling transduction [58]. However, in FGFR3 only the phenylalanine is conserved whereas the

serine is substituted by an alanine, raising the possibility that the C-terminal tail in FGFR3 plays a less significant role in suppressing RTK activity as compared to FGFR2. In support of this notion, truncations resulting in loss of the C-terminal tail lead to constitutive activation of FGFR2 [5,58] but have only marginal impact on FGFR3 activation (**Fig. 4B-F**; Supplementary Fig. S2B-S2E). As delineated in this study, FGFR3 requires both C-tail truncation and fusion to a partner gene that retains the expression of a dimerizing domain to effectively drive oncogenic signaling and tumorigenesis. The presence of a fusion partner may also be necessary for FGFR3$^{\Delta E18}$ to retain the ability to activate PLCγ in a FGFR3 kinase domain-dependent manner, despite lacking the canonical PLCγ-binding site that locates to the proximal C-terminal tail (**Fig. 7B**; Supplementary Fig. S2I and S6A). Taken together, our work highlights how subtle structural differences between the two RTKs may dictate distinct paths towards oncogenic activation.

Collectively, our findings demonstrate divergent behavior of the FGFR2 and FGFR3 paralogs in cancer biology following the loss of the C-terminal tail. Importantly, C-terminally truncated FGFR2 as well as truncated FGFR3 fusions rely on canonical kinase function and are sensitive to FGFRi. Thus, we propose that patients with tumors harboring E18-truncating *FGFR2* alterations or *FGFR3* fusions that engage dimerizing partner genes should be considered for FGFR-targeted therapies.

MATERIALS AND METHODS

Mouse models

To somatically model *Fgfr3* variants in the mouse mammary gland, 6 to 7-week-old female FVB/NRj wild-type (Janvier Labs, RRID:IMSR_RJ:FVB) or in-house bred *Wap-cre;Cdh1*$^{F/F}$ (RRID:MGI:6296605) mice were intraductally injected as previously described [36]. In short, 20 µl of high-titer concentrated lentiviruses (2x10^8-2x10^9 viral particles/ml) encoding *Fgfr3* variants mixed with 0.2% Evans blue dye in PBS were injected into the fourth and/or third mammary glands. Mice were monitored and palpated twice weekly for tumor development. Mammary tumor-free survival was assessed individually for each injected gland upon detection of a palpable tumor (event), while mammary glands that remained tumor-free were censored. Tumor growth was measured in 2D using calipers by applying the following formula: length x width^2 x 0.5. Endpoint was reached when the total mammary tumor burden was a volume of either 1,500mm^3 for a single tumor or 2,000 mm^3 for cumulative tumors or the mice suffered from clinical signs of distress, such as respiratory distress or rapid weight loss. Mice that were euthanized due to clinical signs of distress were censored.

To somatically model *Fgfr3* variants in the mouse lung, high-titer lentiviral vectors encoding *Fgfr3* variants and a *Cre* recombinase were intratracheally delivered via an intubation cannula [59] into the trachea of in-house bred 8 to 12-week-old female/male

FVB *Wap-cre;mTmG* or *Wap-cre;mTmG;P53F* mice. Intratracheal delivery is considered the most direct and consistent method for the virus to reach the lungs. To increase infection efficacy, mice were treated with cyclosporin A orally in the drinking water one week prior to lentiviral infection up until two weeks post infection. Animals were monitored for tumor development every two weeks using non-invasive CT scan-based imaging technology, starting six weeks post lentiviral infection. Mice were sacrificed upon appearance of tumor burden-related clinical symptoms, such as respiratory distress or acute weight loss, which is when a lung tumor-specific survival event was scored.

All tumor measurements and post-mortem analyses were performed in a blinded fashion. The mouse colonies were housed in a certified animal facility with a 12 h light/dark cycle in a temperature-controlled room. Mice were kept in individually ventilated cages, and food and water were provided *ad libitum*. All animal experiments were approved by the Animal Ethics Committee of the Netherlands Cancer Institute under work protocol number 9.2.9125; 9.2.9168; 9.1.9592; 9.1.10022 (AVD3010020172464), 34.1.1140 (AVD30100202316772), 24.1.10061 (AVD30100202011584) and conducted in accordance with institutional, national and European guidelines for Animal Care and Use.

In vivo fexagratinib efficacy and PK/PD studies

DMSO-preserved 1 mm^3 tumor fragments derived from spontaneous tumors driven by *Fgfr3* variants that emerged in the mammary glands of either FVB/NRj wild-type or *Wap-cre;Cdh1*$^{F/F}$ mice were serially transplanted into the mammary fat pad of 8 to 12-week-old FVB/NRj wild-type female mice. Animals were monitored weekly for tumor development and, as soon as tumor pieces showed outgrowth, tumors were measured with a caliper 1-2 times per week. Mice were sacrificed when total tumor burden of 1,500 mm^3 was reached, and tumors were harvested for viable DMSO-biobanking. These DMSO-preserved donor tumor pieces were then used as the starting material for fexagratinib intervention studies and serially transplanted into the mammary fat pad of 8 to 12-week-old female FVB/NRj wild-type mice. For the efficacy study, tumors were grown to a volume of 62.5 mm^3 (5 × 5 mm, measured in 2D using calipers; volume = length × width^2 × 0.5), and animals were randomly allocated to treatment arms. Mice received either vehicle control (1% Tween-80 in demineralized water) or an optimized intermittent dosing schedule of the FGFRi fexagratinib (12.5 mg/kg, AstraZeneca; ref. [26]) as previously described [50]. The treatments were performed daily via oral gavage and mice were euthanized 1 h post the last dosing. For the efficacy or pharmacokinetic-pharmacodynamic (PK/PD) study, tumors were grown to a volume of approximately 170 mm^3 (7 × 7 mm), and animals were randomized to treatment arms. Mice were dosed daily with either vehicle or 12.5 mg/kg fexagratinib for either 2 or 5 consecutive days. Mice were euthanized 1 h post the last dosing, and blood samples were obtained by cardiac puncture using heparinized syringes. Plasma was obtained after centrifugation for 5 min at 5000 x g and kept frozen until analysis. Tumors were excised, weighed and snap-frozen. Prior to analyses, tumors

were fractioned and one part was homogenized in 10 volumes of 1% bovine serum albumin (BSA) in water. Fexagratinib concentrations were measured using an LC-MS/MS method. Calibration samples (range 10 to 10,000 nM) were prepared in human plasma. Volumes of 5 µl of human plasma and 5 µl of mouse plasma samples were vortex-mixed with 60 µl of acetonitrile:formic acid (100:1; v/v), containing 100 nM of buparlisib as internal standard and centrifuged 5 min (20,000 g, 4°C). For tumors, 5 µl of human plasma and 50 µl of tumor homogenate were vortex-mixed with 600 µl of acetonitrile:formic acid (100:1; v/v). Volume of 40 µl of the supernatants were diluted with 160 µl of water and 20 µl was injected on a Zorbax Extend C18 column (100 x 2 mm; ID) using a linear gradient from 20% to 95% methanol in 0.1% formic acid in water at a flow rate of 0.4 ml/min. MS detection was performed in multiple reaction monitoring (MRM) mode using ion pairs 464.3/217.2 for fexagratinib and 411.2/367.2 for buparlisib. The second tumor part was subjected to Western blot PD biomarker analysis (see "Protein isolation and Western blotting").

Histology and immunohistochemistry

Mouse mammary gland and lung tissues were formalin-fixed and paraffin-embedded (FFPE), sectioned and processed for hematoxylin and eosin (H&E) histochemical staining using routine procedures. For mammary gland tissues, E-cadherin immunohistochemistry (IHC) stainings were additionally performed. First, antigen retrieval was achieved with Tris-EDTA at pH 9.0. Next, sections were incubated with anti-E-cadherin primary antibody (see Supplementary Table S1 for details) overnight at 4°C, labeled with EnVision+ HRP Labelled Polymer Anti-Rabbit System (#K4003, Dako; RRID: AB_2630375), visualized with the Liquid DAB+ Substrate Chromogen System (#K3468, Dako), and counterstained with hematoxylin. H&E slides were used to classify mammary and lung lesion types according to the international pathology consensus, and E-cadherin stainings were used to confirm the mammary lesion types. Certified comparative pathologists (S.K., J-Y.S.) evaluated all slides in a blinded fashion.

Lentiviral vectors and virus production

The SIN.LV.SF, SIN.LV.SF-T2A-Puro, SIN.LV.SF-GFP-T2A-Puro and SIN.LV.SF-P2A-Cre lentiviral vectors were previously described [5]. Custom-synthesized gBlocks gene fragments of mouse *Fgfr3* (NM_001163215.2), *Tacc3* (NM_001310541.1), *Add1* (NM_001024458), *Tnip2* (NM_139064) and *Jakmip1* (NM_178394) were purchased (Integrated DNA Technologies). gBlocks gene fragments or parts thereof were assembled in the respective lentivectors using PCR amplification of backbone and insert(s) and the In-Fusion HD Cloning Plus kit (#638911, Takara Bio) according to the manufacturer's recommendations. Point mutations S764A and L772A/L773A in *Tacc3*, and K502R and K644E in *Fgfr3* were generated using the QuikChange Lightning Site-Directed Mutagenesis Kit (#210519, Agilent). The Paircoil2 algorithm [38] was used to annotate the two main CC motifs in the TACC3 protein sequence and to predict the likelihood of their disruption by substituting key leucine (L), valine (V), and/or glutamine (Q) amino acid (AA) residues by prolines (P). Custom-

synthesized gBlocks gene fragments of proline-substituted *Tacc3* variants were purchased (Integrated DNA Technologies) and assembled in the respective lentivectors as described above. Detailed nucleotide and AA sequences are provided in Supplementary Methods S1-S9. In-Fusion and site-directed mutagenesis primers were designed using SnapGene (v.7.0.3; RRID: SCR_015052) and QuikChange Primer Design (https://www.agilent.com/store/primerDesignProgram.jsp; RRID: SCR_025323), respectively. The lentiviral vectors used in this study were all verified by Sanger sequencing. Concentrated (*in vivo*) and unconcentrated (*in vitro*) lentiviral stocks were produced by transient co-transfection of four plasmids in HEK293T cells as previously described [60]. Viral titers were measured with the qPCR Lentivirus Titer Kit (#LV900, Applied Biological Materials).

Cell culture and lentiviral transduction

HEK293T cells (#CRL-3216, ATCC; RRID: CVCL_0063) were cultured in Iscove's Modified Dulbecco Medium (#21980-032, Thermo Fisher Scientific) supplemented with 10% Fetal Bovine Serum (FBS, #FBS-12A, Capricorn Scientific) and 100 IU/ml penicillin and streptomycin (Pen Strep, #15070, Thermo Fisher Scientific). NMuMG mouse mammary epithelial cells (#CRL-1636, ATCC; RRID: CVCL_0075) were cultured in Dulbecco's Modified Eagle Medium/Nutrient Mixture F-12 (DMEM/F-12, #31331-028, Thermo Fisher Scientific) containing 10% FBS and 100 IU/ml Pen Strep. Ba/F3 murine pro B cells (#ACC-300, DSMZ; RRID: CVCL_0161) were cultured in RPMI 1640 medium (#21875-034, Thermo Fisher Scientific) supplemented with 10% FBS, 100 IU/ml Pen Strep and 10 ng/ml recombinant murine IL-3 (#213-13, PeproTech). 5637 human bladder cancer cells (#ACC-35, DSMZ; RRID: CVCL_0126) were cultured in RPMI 1640 medium supplemented with 10% FBS and 100 IU/ml Pen Strep. No re-authentication of the abovementioned cell lines was performed for this study beyond that initially carried out by providers.

To stably express the lentiviral *GFP-T2A-Puro* and *Fgfr3-T2A-Puro* constructs, NMuMG, Ba/F3 and 5637 cells were transduced with lentiviral supernatants at equal multiplicity of infection (MOI) in the presence of 8 µg/ml Polybrene (#H9268, Sigma-Aldrich) for 24 h. Transduced cells were selected with 2 µg/ml Puromycin (#A11138, Thermo Fisher Scientific) for at least 7 days and subsequently grown in medium containing 1 µg/ml Puromycin, with additional 10 µM Y-27632 dihydrochloride (#M1817, AbMole) for the NMuMG cells. All cell lines were cultured in standard incubators at 37 °C with 5% CO_2 and routinely tested for mycoplasma contamination using the MycoAlert Mycoplasma Detection Kit (#LT07-218, Lonza). Experiments were performed with cells cultured for a maximum of 10 passages post lentiviral transduction.

Soft agar anchorage-independent 3D growth assay

Twelve-well plates were precoated with 1 ml of 0.6% low-gelling-temperature agarose (#A9414, Sigma-Aldrich) by diluting 3% agarose solution (in PBS) in DMEM/F-12 supplemented with 3% FBS and Pen Strep. The bottom layer was solidified at 4 °C for 30

min. A single-cell suspension of 30,000 NMuMG cells per well was suspended in 1 ml of 0.3% low-gelling-temperature agarose in DMEM/F-12 supplemented with 3% FBS and Pen Strep, and plated on top. The top layer was solidified at 4 °C for 30 min before transferring the plates to the incubator. The plates were imaged after 20 days using the GelCount colony counter and anchorage-independent growth was quantified using the integrated GelCount colony counting platform (v.1.1.2, Oxford Optronix).

Ba/F3 growth assay upon IL-3 withdrawal

Exponentially growing Ba/F3 cells were washed three times with PBS and seeded in triplicate at 2 x 10^5 cells/ml in the absence of IL-3 supplementation in 12-well plates. Viable cell counts at each time point were obtained using 0.4% tryphan blue (#T8154, Sigma-Aldrich) exclusion on a LUNA-II automated cell counter (Logos Biosystems).

Cell viability assays

5637 parental cells and those expressing *Fgfr3-T2A-Puro* variants were seeded in 12-well plates at 30,000 cells per well. After 24 hr, cells were treated with fexagratinib, afatinib (#HY-10261, MedChem Express), dacomitinib (#HY-13272, MedChem Express) or a combination of afatinib with an anchor concentration of 2.5 μM fexagratinib for 72 hr. Cell viability was measured using CellTiter-Blue reagent (#G808A, Promega) after 1.5-2 hr incubation, and fluorescence was recorded with an Infinite M Plex plate reader (Tecan; RRID:SCR_026522) operated with Tecan i-control software (v.3.9.1; RRID: SCR_024562). Fluorescence values were normalized to untreated control to determine relative viability. Drug-response curves were fitted in GraphPad Prism (v.10.4.1, RRID: SCR_002798) using a four-parameter logistic regression model ([Inhibitor] vs. response, variable slope). For endpoint visualization, cells were fixed with 4% formaldehyde and stained with 0.5% crystal violet in 25% methanol, washed with deionized water, air-dried, and imaged with GelCount (Oxford Optronix; RRID: SCR_023219).

RNA isolation and RT-qPCR

To confirm lentiviral construct overexpression, transduced cells were lysed in RLY buffer (#93594, Bioline) containing 1% of β-mercaptoethanol and total RNA was extracted using the ISOLATE II RNA Mini Kit (#BIO-52073, Bioline) as per manufacturer's instructions. Purified RNA was quantified using the DS-11 Series Spectrophotometer (DeNovix) and 1 μg of total RNA was subjected to reverse transcriptase reaction using the Tetro cDNA Synthesis Kit (#BIO-65042, Bioline) with random hexamer primers. Reverse transcription quantitative PCR (RT-qPCR) was performed using the SensiFAST SYBR Hi-ROX Kit (#BIO-92005, Bioline) and the QuantStudio 6 Flex Real-Time PCR System (#4485691, Thermo Fisher Scientific; RRID: SCR_020239) operated with the QuantStudio Real-Time PCR Software (v.1.7.2, Thermo Fisher Scientific). Primers used were designed using Primer-BLAST (RRID: SCR_003095). Relative quantified cDNA was normalized using the mouse *Usf1* as the housekeeping transcript.

Protein isolation and Western blotting

NMuMG cells stably expressing *GFP* or *Fgfr3* variants were cultured under starvation conditions (0% FBS) for 24 h and, where indicated, treated with 20 ng/ml recombinant human/murine fibroblast growth factor 8b (FGF-8b, #100-25, PeproTech) for 10 min, or 1 μM fexagratinib (AstraZeneca; ref. [26]), 100 nM erdafitinib (#HY-18708, MedChem Express) or 100 nM futibatinib (#HY-100818, MedChem Express) for 3 h. Cells and tumor pieces were lysed in RIPA buffer (50 mM Tris-HCl pH 8.0, 100 mM NaCl, 1 mM EDTA, 1% NP40, 0.5% deoxycholate, and 0.1% SDS in milli-Q water) containing Halt Protease and Phosphatase Inhibitor Cocktail (#78440, Thermo Fisher Scientific) either by pipetting (cells) or using a mechanical homogenizer (tumor pieces). Lysates were cleared by centrifugation at 14,000 rpm for 10 min at 4°C, and protein concentrations were determined with the Pierce BCA Protein Assay Kit (#23225, Thermo Fisher Scientific) using an Infinite 200 PRO plate reader. BlueEye Prestained Protein Marker (#PS-104, Jena Bioscience) and equal amounts of protein were separated on NuPAGE 4-12% Bis-Tris Mini Protein Gels (#NP0323, Thermo Fisher Scientific) using NuPAGE MOPS SDS Running Buffer (#NP0001, Thermo Fisher Scientific), and transferred overnight at 4°C onto Nitrocellulose Membranes (#1620112; Bio-Rad) in transfer buffer (25 mM Tris, 2 M Glycine, 20% methanol in demineralized water). Membranes were stained with Ponceau S (#P7170, Sigma-Aldrich) and imaged with Fusion FX (Vilber), blocked in 5% BSA (#A8022; Sigma-Aldrich) in PBS-T (0.05% Tween-20), and incubated in 5% BSA in PBS-T overnight at 4°C. Membranes were washed in PBS-T and incubated with secondary antibodies in 5% BSA in PBS-T for 1 h at room temperature. Membranes were then washed three times in PBS-T, once in PBS and developed using SuperSignal West Pico PLUS Chemiluminescent Substrate (#34580, Thermo Fisher Scientific), and imaged using Fusion FX operated with the Fusion FX7 Edge imaging system (v.18.05, Vilber). Protein band intensities were measured with mean grey value in Fiji (v.2.14.0, RRID: SCR_002285)[61] and normalized to β-Actin, with phosphoprotein bands being further normalized to corresponding total protein bands. A list of the antibodies used is provided in Supplementary Table S1.

Fluorescence-activated cell sorting

To measure FGFR3 internalization, NMuMG cells expressing *HALO-Fgfr3-T2A-Puro* variants were cultured in DMEM/F12 medium lacking FBS supplementation for 24 hr and treated with 20 ng/ml recombinant human/murine FGF-8b for indicated times. Next, following the surface protein internalization and degradation assay (SPIDA; ref. [33]), cells were sequentially labeled for 15 min each at 37 °C with 350 nM cell membrane impermeable HaloTag ligand (HTL-AF660; #G8471, Promega) and 250 nM cell membrane permeable ligand (HTL-TMR; #G8251, Promega). Cells were then collected with 2 mM EDTA in PBS and labeled with the LIVE/DEAD Fixable Violet Dead Cell Stain Kit (405 nm excitation; #L34955, Thermo Fisher Scientific) and fixed with BD Phosflow Fix Buffer I (#557870, BD Biosciences), at 4 °C for 30 min each. Fluorescence-activated cell sorting (FACS) was performed using a BD LSR II flow cytometer (BD Biosciences, RRID: SCR_002159) operated with BD FACSDiva

Software (v.8.0.1, RRID: SCR_001456). Fluorescence was detected using 450/50, 670/14, and 585/15 bandpass filters to measure LIVE/DEAD viability dye, AF660-HALO-FGFR3, and TMR-HALO-FGFR3, respectively. Data were analyzed with FlowJo (v.10.10.0, BD Biosciences; RRID: SCR_008520) and GraphPad Prism softwares.

Analysis of CGP data from Foundation Medicine

Comprehensive genomic profiling (CGP) was performed on FFPE tumor tissue or blood samples prospectively collected during routine clinical care, as previously described [5]. Briefly, testing was conducted at Foundation Medicine Inc. (FMI), a CLIA-certified, CAP-accredited, New York State-regulated reference laboratory (RRID: SCR_025628). The study was approved by the Western Institutional Review Board (protocol 20152817), with waivers for informed consent and HIPAA authorization. For 217,017 tumor tissue specimens, DNA (>50 ng) was extracted from FFPE specimens, and next-generation sequencing was performed using FoundationOne or FoundationOne CDx testing. This provided high, uniform coverage (>500×) of 315 or 324 cancer-related genes and selected introns of 28 or 36 genes frequently rearranged in cancer [62,63]. Additionally, 26,289 samples were assayed with DNA sequencing for 406 genes and selected introns of 31 genes involved in RE events, along with RNA sequencing (RNA-seq) for 265 genes [64]. For 6,264 liquid samples, plasma was isolated from 20 ml of peripheral whole blood, and at least 20 ng of circulating tumor DNA was extracted [65]. Adapted sequencing libraries were created for the coding exons of 70 genes before hybrid-capture and sample-multiplexed sequencing. Results were analyzed for base substitutions, short insertions and deletions, copy number gains or losses, and REs. The companion diagnostic tests included probes against all *FGFR3* exons and *FGFR3*-I17.

To annotate REs, the location and orientation of both BP sides (*FGFR3* and its partner) were used to determine RE types, as previously described [5]. The gene encoding the longer protein sequence was used as the RE classification backbone. The RE types were defined as follows: (i) in-frame fusion, both BP sides were in the intronic regions of coding genes with in-frame adjacent exons, or both BP sides were in the exonic regions with an in-frame fused sequence; (ii) frame unknown RE, both BP sides were in the intronic regions with at least one out-of-frame adjacent exon, or one or both BP sides were in the exonic regions with an out-of-frame fused sequence; (iii) RE with intergenic space, one BP side was in *FGFR3* and the other in a non-coding intergenic region; (iv) out-of-strand RE, both BP sides were in coding regions, with sense-oriented reads for FGFR3 and antisense-oriented reads for the partner gene; (v) internal RE, both BP sides were within the genomic region of FGFR3; (vi) unresolved RE, the gene upstream to the BP was supported by antisense-oriented read sequences or the REs contained single breakends, which were excluded from the downstream analysis. *FGFR3* amplifications were called if ≥80% of the *FGFR3* targets were at an amplified copy number (CN), defined as ≥4 + median ploidy of the sample. Differential CN gains of E18 targets < E1-E17 targets were defined as *FGFR3*-E1-E17 partial

amplifications. In samples with *FGFR3* REs and co-amplification, low-level REs were discarded at a read threshold dependent on the amplification CN. Nonsense, frameshift, and splice-site mutations in E18 were defined as *FGFR3* E18-truncating mutations.

Analysis of self-interacting capacity among FGFR3 RE partners

The SLIPPER algorithm was used to obtain proteins with self-interacting capacity [27]. The SLIPPER algorithm, trained on seven proteome databases (DIP, IntAct, MINT, BioGRID, PDB, MatrixDB and 12D), established the SLIPPER golden standard dataset of potentially self-interacting proteins. Using this dataset, the proportion of self-interactors among unique proteins encoded by *FGFR3* RE partner genes in the FMI dataset was calculated. To identify specific self-interacting domains in E18-truncated *FGFR3* RE partners, domain-domain interaction data were obtained from 3did [66] and PPIDM [67] databases. Proteins containing coiled-coil domains were obtained from the UniProt database (release 2021_04). Two-tailed Fisher's exact test was performed to statistically compare the proportion of self-interacting proteins and proteins with coiled-coil domains.

Analysis of WGS data from the HMF

Preprocessed whole genome sequencing (WGS) data on metastatic solid tumors were obtained from the Hartwig Medical Foundation (HMF; data access request DR-205) via their Google Cloud computing platform. The data were preprocessed using their bioinformatics pipeline, designed to detect all types of somatic alterations, including structural variants and CN alterations (CNAs; https://github.com/hartwigmedical/pipeline5). In brief, sequencing reads were mapped to the human reference genome GRCh37 using Burrows-Wheeler Alignment (BWA-MEM, v.0.7.5a; ref. [68]). Somatic structural variants were identified with GRIDSS (v.1.8.0; ref. [69]), and CNAs and tumor purity were estimated using PURPLE (v.2.43, RRID: SCR_022999; ref. [10]). LINX (v.1.9; ref. [70]) was then used to annotate events and construct derivative chromosome structures. Based on the PURPLE output, samples containing structural variant BPs within the *FGFR3* genomic region were selected for further structural variant analysis. To annotate structural variants, the location and orientation of both BP sides (*FGFR3* and its partner) were used to determine RE types as described for the FMI panel-seq data. *FGFR3* CN gains of >5 were defined as amplifications. Among the samples with *FGFR3* CN segment BPs at I17/E18, samples with E1-E17 CN ($CN_{E1–E17}$) > 5 and $CN_{E1–E17}$-CN_{E18} > 2 were defined as *FGFR3*-E1-E17 partially amplified.

Analysis of RNA-seq data from the HMF

Raw RNA-seq data (fastq files) on metastatic solid tumors were obtained from the HMF (data access request DR-205). Sequencing reads were mapped to the human reference genome GRCh38 (Gencode v32 CTAT) using STAR (v.2.7.2; ref. [71]) with the recommended parameters. These mapped reads were then used to run STAR-Fusion (v.1.8.1; RRID: SCR_025853; ref. [72]). STAR-Fusion was executed with the chimeric alignment information (Chimeric.out.junction) obtained from STAR and GRCh38 Gencode v32 CTAT. Chimeric

alignments from STAR and gene fusions from STAR-Fusion were inspected to identify RNA-seq alignments supporting the REs identified in WGS. For samples with in-frame fusions identified in WGS, the upstream and downstream exon numbers of the fusion gene, inferred from STAR-Fusion, were matched to the fusion found in WGS. For samples with other types of REs identified in WGS, chimeric reads spanning the upstream exon and the downstream exon (out-of-frame REs), the downstream intergenic sequence (REs with intergenic space), or the downstream antisense gene sequence (out-of-strand REs) were mined from the 'Chimeric.out.junction' file and matched to the REs found in WGS. Genome coordinates were converted from GRCh37 to GRCh38 using UCSC Lift Genome Annotations (https://genome.ucsc.edu/cgi-bin/hgLiftOver). IGV (v.1.11.0, RRID: SCR_011793; ref. [73]) was used to generate sashimi plots.

Statistical analysis and reproducibility

Data of *in vitro* and *in vivo* experiments were analyzed using Prism (v.10.0.3, GraphPad Software; RRID: SCR_002798) and ClustVis (v.2.0, RRID: SCR_017133; ref. [74]). Genomic data were analyzed using R (v. 4.3.3, RRID: SCR_001905). *In vitro* experiments were independently repeated at least twice, and all attempts at replication were successful. Sample sizes of mouse cohorts were based on previous calculations [5] or determined using the Sample Size Calculator (http://powerandsamplesize.com/Calculators) and were large enough to measure the effect sizes. Data were reproducible across batches analyzed, and all attempts at replication were successful. The statistical tests used are described in the corresponding figure legends. $P < 0.05$ was considered statistically significant. Exact P values are always disclosed in the corresponding figure panels.

Data availability

Preprocessed WGS and raw RNA-seq data from the HMF were downloaded from their Google Cloud computing platform under data-sharing agreement DR-205. These data can be obtained through standardized procedures and request forms available online (https://www.hartwigmedicalfoundation.nl/en/). CGP data can be obtained from FMI on reasonable request (https://www.foundationmedicine.com/service/genomic-data-solutions). The human reference genome (GRCh38 Gencode v32 CTAT) used for RNA-seq data analysis is available in CTAT Genome Lib data resources (https://data.broadinstitute.org/Trinity/CTAT_RESOURCE_LIB). Domain–domain interaction information from 3did and PPIDM are available online (https://3did.irbbarcelona.org and http://ppidm.loria.fr, respectively). The code used in this study can be found at Code Ocean (https://codeocean.com/capsule/5476052/tree/v1). All other raw data generated in this study are available upon request from the corresponding authors.

Code availability

WGS data from the HMF were analyzed using published computer codes (https://github.com/hartwigmedical/pipeline5) including BWA-MEM, GRIDSS, PURPLE and LINX to detect

all types of somatic alterations, including structural variants and CNAs. Codes used for analyzing *FGFR3* RE types and partners are deposited at https://github.com/bynjh007/FGFR3_RE_analysis.

Conflicts of interest

J.K.L. is an employee of Foundation Medicine, Inc. and has equity in Roche. J.S.R. is an employee of Foundation Medicine, Inc., has equity in Roche, and is a board member of Celsius Therapeutics. S.G. has received research funding from M2Gen, has equity in Inspirata and Silagene, and has consulted for Foghorn Therapeutics, Foundation Medicine, Inspirata, Merck, Novartis, Roche and Silagene; his spouse is an employee of and has equity in Merck. D.Z. is an employee of Genentech, Inc. and has equity in Roche. The other authors declare no potential conflicts of interest.

Acknowledgments

We thank H. van der Gulden for support with cloning, F. van Diepen for assistance with FACS, and the NKI animal facility, animal pathology facility and Mouse Cancer Clinic for their technical support in performing the animal experiments. This publication and the underlying study have been made possible in part on the basis of data provided by HMF and the Center of Personalised Cancer Treatment (CPCT).

Research at the NKI is supported by institutional grants of the Dutch Cancer Society and the Dutch Ministry of Health, Welfare and Sport. This work is part of the Oncode Institute, which is partly financed by the Dutch Cancer Society. This work was funded by the Dutch Cancer Society (KWF grants 7835 and 12894). This work was also supported by National Research Foundation of Korea (NRF) grants (MSIT; RS-2024-00342142 and RS-2023-00261820) and a faculty research grant of Yonsei University College of Medicine (6-2024-0041).

Author contributions

J.Y., J.B., D.Z., and J.J. conceived the ideas and designed the experiments. J.Y., C.L., L.D., E.W., S.A., and O.v.T. performed the laboratory experiments. J.Y., A.P.D., E.v.d.B., N.P., B.S., and D.Z. conceived and performed the animal experiments. S.K. and J.-Y.S. assessed the histology of mouse tumors. J.B. and H.M. performed the bioinformatic analyses. J.K.L. and J.S.R. provided the Foundation Medicine data. J.Y., J.B., S.G., L.F.A.W., D.Z. and J.J. supervised the bioinformatic analyses and the laboratory experiments. M.v.d.V. supervised the animal experiments. J.Y., J.B., D.Z., and J.J. wrote the manuscript.

Online content

The supplementary data for this article, including Supplementary Tables S1-S2, Supplementary Data S1-S2 and Supplementary Methods S1-S9 are available at https://doi.org/10.1158/0008-5472.CAN-24-2648.

REFERENCES

1. Helsten, T. *et al.* (2016) The FGFR landscape in cancer: Analysis of 4,853 tumors by next-generation sequencing. *Clin. Cancer Res.* 22, 259–267
2. Murugesan, K. *et al.* (2022) Pan-tumor landscape of fibroblast growth factor receptor 1-4 genomic alterations. *ESMO Open* 7, 100641
3. Sun, Y. *et al.* (2020) A comprehensive pan-cancer study of fibroblast growth factor receptor aberrations in Chinese cancer patients. *Ann. Transl. Med.* 8, 1290–1290
4. Katoh, M. *et al.* (2024) FGFR-targeted therapeutics: clinical activity, mechanisms of resistance and new directions. *Nat. Rev. Clin. Oncol.* DOI: 10.1038/s41571-024-00869-z
5. Zingg, D. *et al.* (2022) Truncated FGFR2 is a clinically actionable oncogene in multiple cancers. *Nature* 608, 609–617
6. Rodón, J. *et al.* (2024) Pemigatinib in previously treated solid tumors with activating FGFR1–FGFR3 alterations: phase 2 FIGHT-207 basket trial. *Nat. Med.* DOI: 10.1038/s41591-024-02934-7
7. Wu, Y.M. *et al.* (2013) Identification of targetable FGFR gene fusions in diverse cancers. *Cancer Discov.* 3, 636–647
8. Qin, A. *et al.* (2019) Detection of Known and Novel FGFR Fusions in Non–Small Cell Lung Cancer by Comprehensive Genomic Profiling. *J. Thorac. Oncol.* 14, 54–62
9. Turner, N. and Grose, R. (2010) Fibroblast growth factor signalling: From development to cancer. *Nat. Rev. Cancer* 10, 116–129
10. Priestley, P. *et al.* (2019) Pan-cancer whole-genome analyses of metastatic solid tumours. *Nature* 575, 210–216
11. Costa, R. *et al.* (2016) FGFR3-TACC3 fusion in solid tumors: Mini review. *Oncotarget* 7, 55924–55938
12. Mata, D.A. *et al.* (2020) Genetic and epigenetic landscape of IDH-wildtype glioblastomas with FGFR3-TACC3 fusions. *Acta Neuropathol. Commun.* 8, 186
13. Singh, D. *et al.* (2012) Transforming fusions of FGFR and TACC genes in human glioblastoma. *Science* 337, 1231–1235
14. Di Stefano, A.L. *et al.* (2015) Detection, characterization, and inhibition of FGFR-TACC fusions in IDH wild-type glioma. *Clin. Cancer Res.* 21, 3307–3317
15. Parker, B.C. *et al.* (2013) The tumorigenic FGFR3-TACC3 gene fusion escapes miR-99a regulation in glioblastoma. *J. Clin. Invest.* 123, 855
16. Bao, Z.-S. *et al.* (2014) RNA-seq of 272 gliomas revealed a novel, recurrent PTPRZ1-MET fusion transcript in secondary glioblastomas. *Genome Res.* 24, 1765–1773
17. Williams, S.V. *et al.* (2013) Oncogenic FGFR3 gene fusions in bladder cancer. *Hum. Mol. Genet.* 22, 795–803
18. Best, S.A. *et al.* (2018) FGFR3-TACC3 is an oncogenic fusion protein in respiratory epithelium. *Oncogene* 37, 6096–9104
19. Majewski, I.J. *et al.* (2013) Identification of recurrent FGFR3 fusion genes in lung cancer through kinome-centred RNA sequencing. *J. Pathol.* 230, 270–276
20. Capelletti, M. *et al.* (2014) Identification of recurrent FGFR3-TACC3 fusion oncogenes from lung adenocarcinoma. *Clin. Cancer Res. Off. J. Am. Assoc. Cancer Res.* 20, 6551–6558
21. Wang, R. *et al.* (2014) FGFR1/3 tyrosine kinase fusions define a unique molecular subtype of non-small cell lung cancer. *Clin. Cancer Res.* 20, 4107–4114
22. Kim, Y. *et al.* (2014) Integrative and comparative genomic analysis of lung squamous cell carcinomas in East Asian patients. *J. Clin. Oncol. Off. J. Am. Soc. Clin. Oncol.* 32, 121–128
23. Shaver, T.M. *et al.* (2016) Diverse, Biologically Relevant, and Targetable Gene Rearrangements in Triple-Negative Breast Cancer and Other Malignancies. *Cancer Res.* 76, 4850–4860

24. Chew, N.J. *et al.* (2020) FGFR3 signaling and function in triple negative breast cancer. *Cell Commun. Signal.* 18, 1–17
25. Nozad, S. *et al.* (2017) Comprehensive genomic profiling of malignant phyllodes tumors of the breast. *Breast Cancer Res. Treat.* 162, 597–602
26. Gavine, P.R. *et al.* (2012) AZD4547: an orally bioavailable, potent, and selective inhibitor of the fibroblast growth factor receptor tyrosine kinase family. *Cancer Res.* 72, 2045–2056
27. Liu, Z. *et al.* (2013) Proteome-wide prediction of self-interacting proteins based on multiple properties. *Mol. Cell. Proteomics MCP* 12, 1689–1700
28. Horibata, S. *et al.* (2015) Utilization of the Soft Agar Colony Formation Assay to Identify Inhibitors of Tumorigenicity in Breast Cancer Cells. *J. Vis. Exp. JoVE* DOI: 10.3791/52727
29. Warmuth, M. *et al.* (2007) Ba/F3 cells and their use in kinase drug discovery. *Curr. Opin. Oncol.* 19, 55–60
30. Nelson, K.N. *et al.* (2016) Oncogenic gene fusion FGFR3-TACC3 Is regulated by tyrosine phosphorylation. *Mol. Cancer Res.* 14, 458–469
31. Szybowska, P. *et al.* (2021) Negative Regulation of FGFR (Fibroblast Growth Factor Receptor) Signaling. *Cells* 10, 1342
32. Bache, K.G. *et al.* (2004) Defective downregulation of receptor tyrosine kinases in cancer. *EMBO J.* 23, 2707–2712
33. Stüber, J.C. *et al.* (2019) High-Throughput Quantification of Surface Protein Internalization and Degradation. *ACS Chem. Biol.* 14, 1154–1163
34. Ciriello, G. *et al.* (2015) Comprehensive Molecular Portraits of Invasive Lobular Breast Cancer. *Cell* 163, 506–519
35. Derksen, P.W.B. *et al.* (2011) Mammary-specific inactivation of E-cadherin and p53 impairs functional gland development and leads to pleomorphic invasive lobular carcinoma in mice. *Dis. Model. Mech.* 4, 347–358
36. Annunziato, S. *et al.* (2016) Modeling invasive lobular breast carcinoma by CRISPR/Cas9-mediated somatic genome editing of the mammary gland. *Genes Dev.* 30, 1470–1480
37. Kas, S.M. *et al.* (2017) Insertional mutagenesis identifies drivers of a novel oncogenic pathway in invasive lobular breast carcinoma. *Nat. Genet.* 49, 1219–1230
38. McDonnell, A.V. *et al.* (2006) Paircoil2: improved prediction of coiled coils from sequence. *Bioinforma. Oxf. Engl.* 22, 356–358
39. Kinoshita, K. *et al.* (2005) Aurora A phosphorylation of TACC3/maskin is required for centrosome-dependent microtubule assembly in mitosis. *J. Cell Biol.* 170, 1047–1055
40. Fu, W. *et al.* (2013) Self-assembly and sorting of acentrosomal microtubules by TACC3 facilitate kinetochore capture during the mitotic spindle assembly. *Proc. Natl. Acad. Sci. U. S. A.* 110, 15295–15300
41. Schneider, L. *et al.* (2007) The transforming acidic coiled coil 3 protein is essential for spindle-dependent chromosome alignment and mitotic survival. *J. Biol. Chem.* 282, 29273–29283
42. Gergely, F. *et al.* (2003) The ch-TOG/XMAP215 protein is essential for spindle pole organization in human somatic cells. *Genes Dev.* 17, 336–341
43. Yao, R. *et al.* (2007) TACC3 is required for the proper mitosis of sclerotome mesenchymal cells during formation of the axial skeleton. *Cancer Sci.* 98, 555–562
44. Peset, I. *et al.* (2005) Function and regulation of Maskin, a TACC family protein, in microtubule growth during mitosis. *J. Cell Biol.* 170, 1057–1066
45. Lioutas, A. and Vernos, I. (2013) Aurora A kinase and its substrate TACC3 are required for central spindle assembly. *EMBO Rep.* 14, 829–836
46. Ulisse, S. *et al.* (2007) Transforming acidic coiled-coil 3 and Aurora-A interact in human thyrocytes and their expression is deregulated in thyroid cancer tissues. *Endocr. Relat. Cancer* 14, 827–837

47. Ding, Z.M. *et al.* (2017) The role of TACC3 in mitotic spindle organization. *Cytoskeleton* 74, 369–378
48. Hood, F.E. *et al.* (2013) Coordination of adjacent domains mediates TACC3-ch-TOG-clathrin assembly and mitotic spindle binding. *J. Cell Biol.* 202, 463–478
49. Nelson, K.N. *et al.* (2018) Oncogenic driver FGFR3-TACC3 is dependent on membrane trafficking and ERK signaling. *Oncotarget* 9, 34306–34319
50. Kas, S.M. *et al.* (2018) Transcriptomics and transposon mutagenesis identify multiple mechanisms of resistance to the FGFR inhibitor AZD4547. *Cancer Res.* 78, 5668–5679
51. Katoh, M. (2019) Fibroblast growth factor receptors as treatment targets in clinical oncology. *Nat. Rev. Clin. Oncol.* 16, 105–122
52. Juric, D. *et al.* (2025) PI3Kα inhibitor and degrader inavolisib can co-opt FGFR2 to enhance responses in patients with PIK3CA-mutated solid tumors and in preclinical models. *Clin. Cancer Res.* DOI: 10.1158/1078-0432.CCR-25-1459
53. Silverman, I.M. *et al.* (2021) Clinicogenomic Analysis of FGFR2-Rearranged Cholangiocarcinoma Identifies Correlates of Response and Mechanisms of Resistance to Pemigatinib. *Cancer Discov.* 11, 326–339
54. D'Souza, N. *et al.* (2024) Comutational patterns in FGFR3-altered non-muscle invasive bladder cancer influence recurrence and progression. *Urol. Oncol. Semin. Orig. Investig.* 42, S55
55. Wang, C.G. *et al.* (2023) Oncogenic driver FGFR3-TACC3 requires five coiled-coil heptads for activation and disulfide bond formation for stability. *Oncotarget* 14, 133
56. Parker, B.C. *et al.* (2014) Emergence of FGFR family gene fusions as therapeutic targets in a wide spectrum of solid tumours. *J. Pathol.* 232, 4–15
57. Sarkar, S. *et al.* (2017) FGFR3-TACC3 cancer gene fusions cause mitotic defects by removal of endogenous TACC3 from the mitotic spindle. *Open Biol.* 7
58. Zingg, D. *et al.* (2025) The C-Terminal Kinase Domain–Binding and Suppression Motif Prevents Constitutive Activation of FGFR2. *Cancer Res.* 85, 3234–3257
59. DuPage, M. *et al.* (2009) Conditional mouse lung cancer models using adenoviral or lentiviral delivery of Cre recombinase. *Nat. Protoc.* 4, 1064–1072
60. Dull, T. *et al.* (1998) A third-generation lentivirus vector with a conditional packaging system. *J. Virol.* 72, 8463–8471
61. Schindelin, J. *et al.* (2012) Fiji: an open-source platform for biological-image analysis. *Nat. Methods* 9, 676–682
62. Frampton, G.M. *et al.* (2013) Development and validation of a clinical cancer genomic profiling test based on massively parallel DNA sequencing. *Nat. Biotechnol.* 31, 1023–1031
63. Milbury, C.A. *et al.* (2022) Clinical and analytical validation of FoundationOne®CDx, a comprehensive genomic profiling assay for solid tumors. *PloS One* 17, e0264138
64. He, J. *et al.* (2016) Integrated genomic DNA/RNA profiling of hematologic malignancies in the clinical setting. *Blood* 127, 3004–3014
65. Clark, T.A. *et al.* (2018) Analytical Validation of a Hybrid Capture-Based Next-Generation Sequencing Clinical Assay for Genomic Profiling of Cell-Free Circulating Tumor DNA. *J. Mol. Diagn. JMD* 20, 686–702
66. Stein, A. *et al.* (2005) 3did: interacting protein domains of known three-dimensional structure. *Nucleic Acids Res.* 33, D413-417
67. Alborzi, S.Z. *et al.* (2021) PPIDomainMiner: Inferring domain-domain interactions from multiple sources of protein-protein interactions. *PLoS Comput. Biol.* 17, e1008844
68. Li, H. and Durbin, R. (2009) Fast and accurate short read alignment with Burrows-Wheeler transform. *Bioinformatics* 25, 1754–1760
69. Cameron, D.L. *et al.* (2017) GRIDSS: sensitive and specific genomic rearrangement detection using positional de Bruijn graph assembly. *Genome Res.* 27, 2050–2060

70. Shale, C. *et al.* (2022) Unscrambling cancer genomes via integrated analysis of structural variation and copy number. *Cell Genomics* 2, 100112
71. Dobin, A. *et al.* (2013) STAR: Ultrafast universal RNA-seq aligner. *Bioinformatics* 29, 15–21
72. Haas, B.J. *et al.* (2019) Accuracy assessment of fusion transcript detection via read-mapping and de novo fusion transcript assembly-based methods. *Genome Biol.* 20, 213
73. Robinson, J.T. *et al.* (2011) Integrative genomics viewer. *Nat. Biotechnol.* 29, 24–26
74. Metsalu, T. and Vilo, J. (2015) ClustVis: a web tool for visualizing clustering of multivariate data using Principal Component Analysis and heatmap. *Nucleic Acids Res.* 43, W566-570

SUPPLEMENTARY FIGURES

A

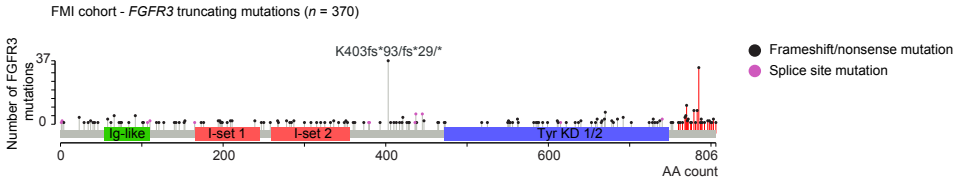

B

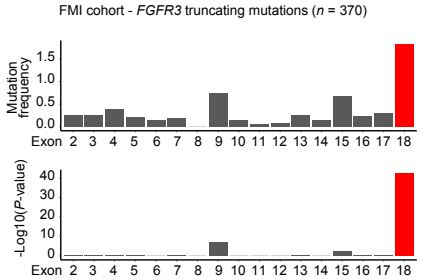

C

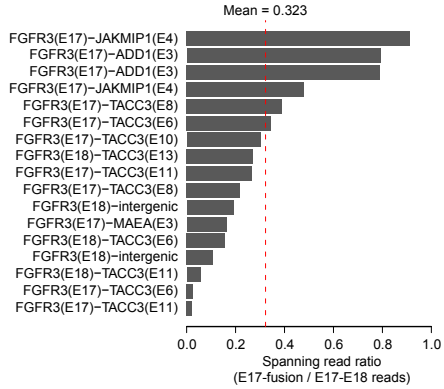

Supplementary Figure S1. Genomic alterations affecting *FGFR3*.

A,B, Lollipop plot (**A**) and normalized frequency (top panel) and enrichment significance (*P* values, bottom panel) (**B**) of *FGFR3*-truncating mutations identified in the FMI cohort. Mutation frequency was normalized by the kilobase of exon length and total number of mutations. AA, amino acid; in red, mutations affecting E18. **C,** Ratio of *FGFR3* junction reads spanning from E17 to E18 (E17-E18) versus E17-fusion partners (E17-fusion) for 17 of the RNA-seq profiles available from the HMF cohort.

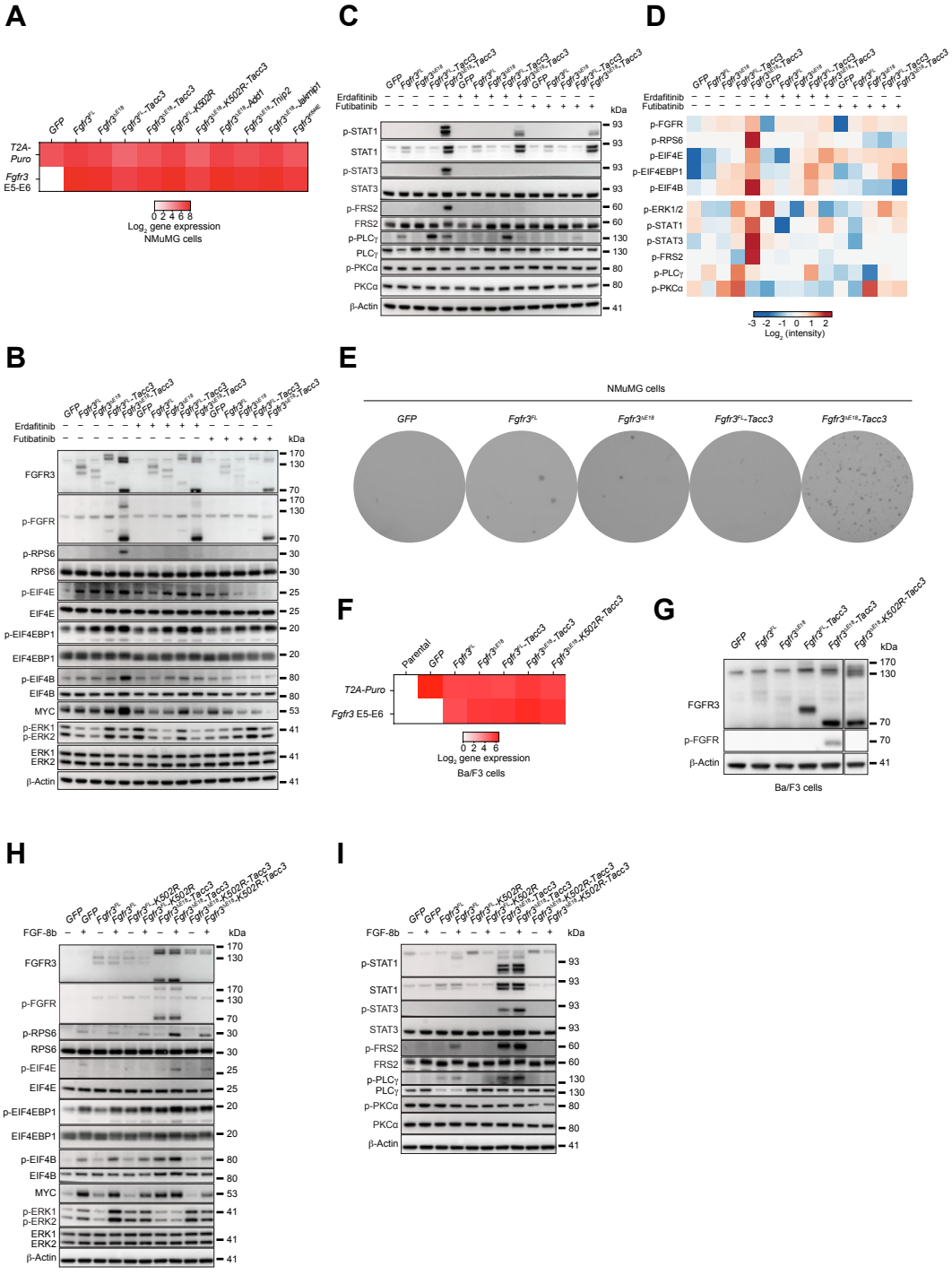
A
GFP
Fgfr3FL
Fgfr3E18
Fgfr3FL-Tacc3
Fgfr3E18-Tacc3
Fgfr3FL-K502R
Fgfr3E18-K502R-Tacc3
Fgfr3E18-Adtrl
Fgfr3E18-Tnip2
Fgfr3E18-Jakmip1
Fgfr3mMe
T2A-Puro
Fgfr3 E5-E6
0 2 4 6 8
Log2 gene expression
NMuMG cells
B
Erdafitinib
Futibatinib
kDa
FGFR3
p-FGFR
p-RPS6
RPS6
p-EIF4E
EIF4E
p-EIF4EBP1
EIF4EBP1
p-EIF4B
EIF4B
MYC
p-ERK1
p-ERK2
ERK1
ERK2
β-Actin
C
p-STAT1
STAT1
p-STAT3
STAT3
p-FRS2
FRS2
p-PLCγ
PLCγ
p-PKCα
PKCα
β-Actin
D
p-FGFR
p-RPS6
p-EIF4E
p-EIF4EBP1
p-EIF4B
p-ERK1/2
p-STAT1
p-STAT3
p-FRS2
p-PLCγ
p-PKCα
-3 -2 -1 0 1 2
Log2 (intensity)
E
NMuMG cells
GFP
Fgfr3FL
Fgfr3E18
Fgfr3FL-Tacc3
Fgfr3E18-Tacc3
F
Parental
T2A-Puro
Fgfr3 E5-E6
0 2 4 6
Log2 gene expression
Ba/F3 cells
G
Fgfr3E18-K502R-Tacc3
FGFR3
p-FGFR
β-Actin
Ba/F3 cells
H
FGF-8b
I

Supplementary Figure S2. Expression, FGFR3 pathway inhibition/activation, and transforming potential of *Fgfr3* variants in NMuMG and Ba/F3 cell models.

A, Validation of the overexpression of *Fgfr3* variants in NMuMG cells using RT-qPCR. T2A–Puro primers specifically detect *Fgfr3* transcripts derived from lentiviral constructs, *Fgfr3* E4–E5 primers (spanning the exon junction of exons 4 and 5 of *Fgfr3*) detect both endogenous transcripts and those derived from lentiviral constructs. Log2-transformed expression of each cDNA segment is normalized to *Usf1* housekeeping gene expression. Data are represented as mean of $n = 3$ technical replica per group of 1 experiment. **B, C,** Western blots showing expression and phosphorylation of indicated proteins in 24 hr serum-starved NMuMG cells stably expressing *GFP*, *Fgfr3*^{FL}, *Fgfr3*$^{\Delta E18}$, *Fgfr3*^{FL}*-Tacc3*, or *Fgfr3*$^{\Delta E18}$*-Tacc3* and treated for 3 hr with 100 nM erdafitinib or 100 nM futibatinib. β-Actin was run as sample processing control and is duplicated in (**B, C**). Weights of protein marker bands (kDa) are indicated. **D,** Quantifications of indicated phosphoprotein band intensities based on Western blots in (**B, C**). Phospho band intensities were normalized to their individual lane backgrounds and to their corresponding total protein band intensities and β-actin bands. **E,** Representative images of 12-well plate wells of 3D soft agar colony formation assay using NMuMG cells stably expressing *GFP*, *Fgfr3*^{FL}, *Fgfr3*$^{\Delta E18}$, *Fgfr3*^{FL}*-Tacc3*, or *Fgfr3*$^{\Delta E18}$*-Tacc3* and grown for 20 days. **F**, Validation of the overexpression of *Fgfr3* variants in Ba/F3 cells using RT-qPCR. Primers and analysis strategy used was the same as in (**A**). **G**, Western blots showing FGFR3 and phosphorylated FGFR protein expression in Ba/F3 cells stably expressing *GFP*, *Fgfr3*^{FL}, *Fgfr3*$^{\Delta E18}$, *Fgfr3*^{FL}*-Tacc3*, *Fgfr3*$^{\Delta E18}$*-Tacc3* or *Fgfr3*$^{\Delta E18}$*-K502R-Tacc3*. β-Actin was run as sample processing control. Intermediate lanes containing samples not relevant to this figure were removed for clarity during image processing. A gap indicates where the blot was cropped, but all samples shown were run on the same gel and processed under identical conditions. No other alterations were made. **H, I,** Western blots showing expression and phosphorylation of indicated proteins in 24 hr serum-starved NMuMG cells stably expressing *GFP*, *Fgfr3*^{FL}, *Fgfr3*^{FL}*-K502R*, *Fgfr3*$^{\Delta E18}$*-Tacc3* or *Fgfr3*$^{\Delta E18}$*-K502R-Tacc3* and treated for 10 min with 20 ng/ml FGF-8b. β-Actin was run as sample processing control and is duplicated in (**H, I**). Molecular weights of protein marker bands in (**B**, **C**, **G-I**) are indicated in kDa, and all blots were stained with Ponceau S to ensure equal loading of total protein.

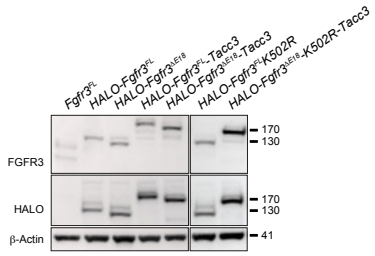

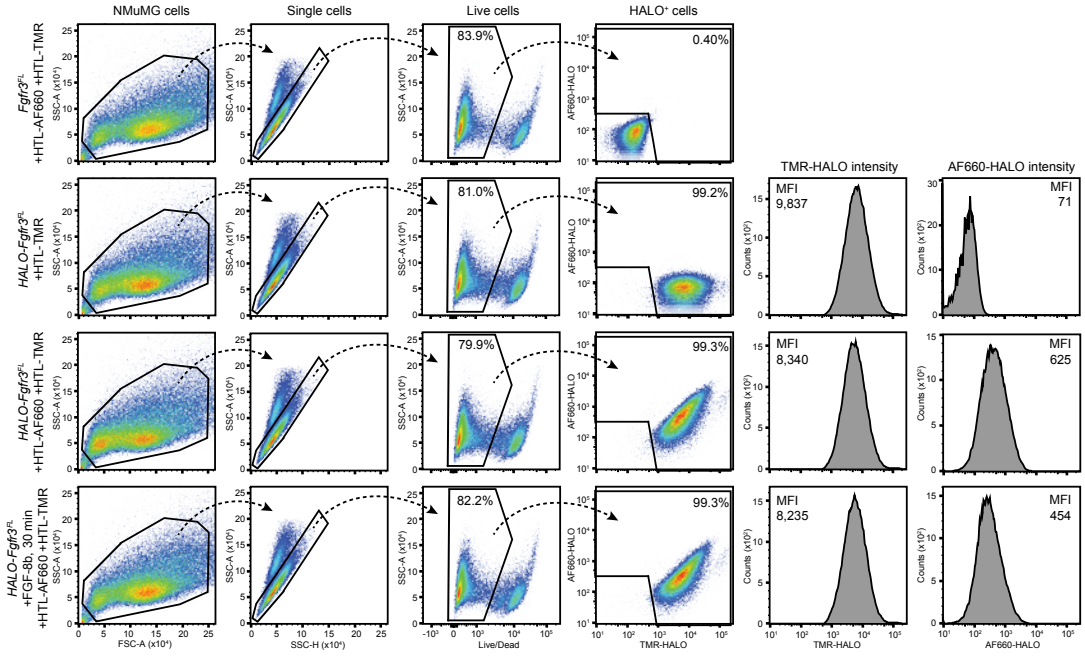

Supplementary Figure S3. Measurements of HALO-FGFR3 internalization.

A, Western blots showing expression of HALO-FGFR3 in NMuMG cells expressing *Fgfr3* or indicated *HALO-Fgfr3* variants used to perform the SPIDA assay. β-Actin was run as sample processing control on the same blot as FGFR3, and weights of protein marker bands (kDa) are indicated. **B,** FACS gating strategy used to quantify surface and internal HALO-tagged FGFR3 in serum-starved NMuMG cells expressing *Fgfr3*^{FL} or *HALO-Fgfr3*^{FL} constructs following the SPIDA assay. Where applicable, cells were stimulated with 20 ng/ml FGF-8b and sequentially labeled with a cell-impermeable HaloTag ligand conjugated to AF660, followed by a cell permeable HaloTag ligand conjugated to TMR. Gating was performed as follows: (i) FSC-A vs. SSC-A to identify the main cell population and exclude debris, (ii) SSC-H vs. SSC-A to isolate single cells, (iii) Live/Dead vs. SSC-A to gate live cells, and (iv) TMR-HALO vs. AF660-HALO to select for HALO-positive cells. Median fluorescence intensity (MFI) of AF660 and TMR signals was then quantified to assess surface-localized and internalized HALO-tagged FGFR3, respectively.

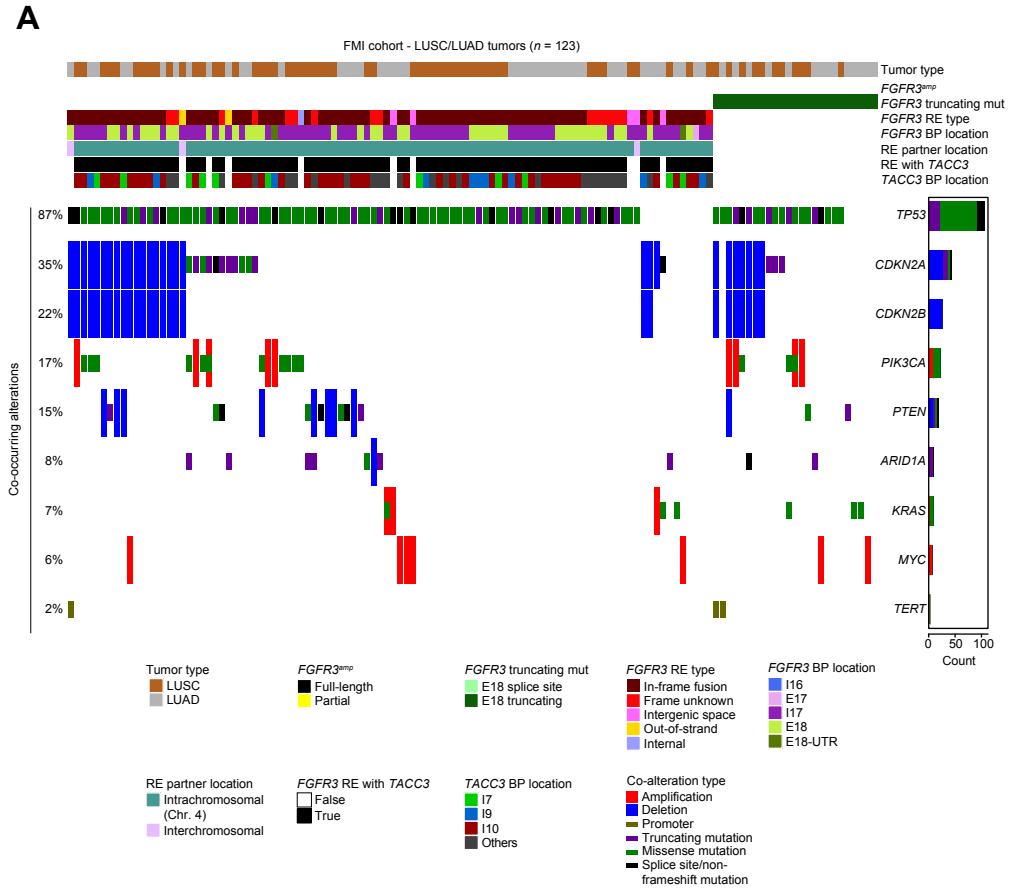

Supplementary Figure S4. Top driver genes co-occurring in human lung cancers with *FGFR3* E18 truncations, and histological examination of mouse lungs injected with *Fgfr3* variants.

A, Analysis of 123 LUSC/LUAD tumors (0.049% incidence) carrying potential *FGFR3* E18 truncations identified among 249,570 pan-cancer diagnostic hybrid-capture panel-seq profiles derived from FMI. These samples include *FGFR3* REs with BPs at the C-terminal tail, E17/18 or I16/17, or *FGFR3*-E18 truncating mutations. *FGFR3* REs consist of in-frame fusions, frame-unknown REs, intergenic space REs, out-of-strand REs, and internal REs. Tumor type, *FGFR3* amplification status, BP location of *FGFR3*, RE partner location, and REs with *TACC3* and its corresponding BP location are indicated. Top-9 co-occurring tumor driver genes and their corresponding alteration type are shown. **B,** Lung tumor type classifications of *Fgfr3* somatic mouse models based on hematoxylin and eosin (H&E) stainings. Cohort counts (*n*) represent evaluated mammary glands per number of mice.

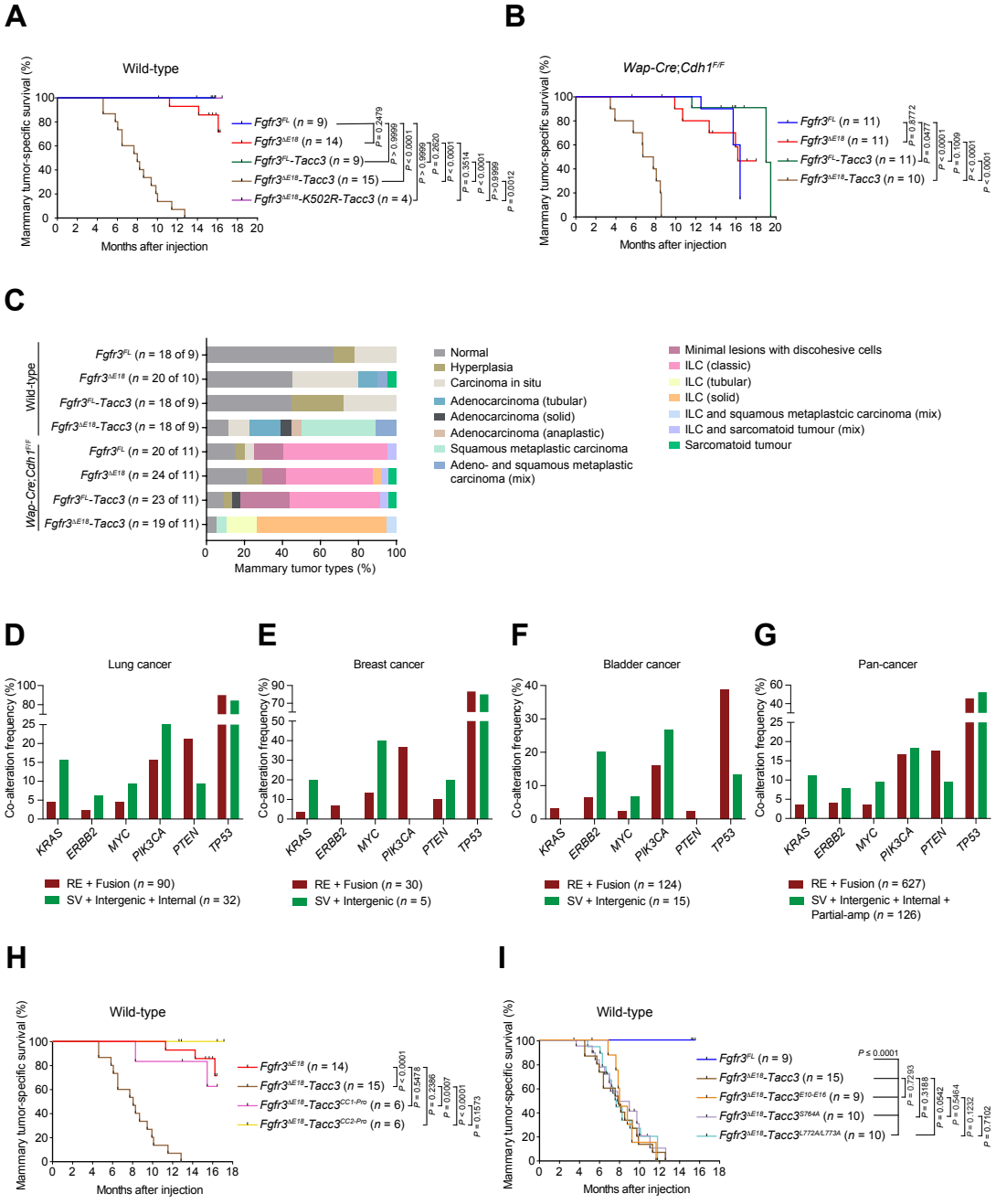
A
Wild-type
Mammary tumor-specific survival (%)
Months after injection
Fgfr3FL (n = 9)
Fgfr3ΔE18 (n = 14)
Fgfr3FL-Tacc3 (n = 9)
Fgfr3ΔE18-Tacc3 (n = 15)
Fgfr3ΔE18-K502R-Tacc3 (n = 4)
P = 0.2479
P > 0.9999
P < 0.0001
P > 0.9999
P = 0.2620
P < 0.0001
P = 0.3514
P < 0.0001
P > 0.9999
P = 0.0012
B
Wap-Cre;Cdh1F/F
Mammary tumor-specific survival (%)
Months after injection
Fgfr3FL (n = 11)
Fgfr3ΔE18 (n = 11)
Fgfr3FL-Tacc3 (n = 11)
Fgfr3ΔE18-Tacc3 (n = 10)
P = 0.8772
P = 0.0477
P < 0.0001
P = 0.1009
P < 0.0001
P < 0.0001
C
Wild-type
Wap-Cre;Cdh1F/F
Fgfr3FL (n = 18 of 9)
Fgfr3ΔE18 (n = 20 of 10)
Fgfr3FL-Tacc3 (n = 18 of 9)
Fgfr3ΔE18-Tacc3 (n = 18 of 9)
Fgfr3FL (n = 20 of 11)
Fgfr3ΔE18 (n = 24 of 11)
Fgfr3FL-Tacc3 (n = 23 of 11)
Fgfr3ΔE18-Tacc3 (n = 19 of 11)
Mammary tumor types (%)
Normal
Hyperplasia
Carcinoma in situ
Adenocarcinoma (tubular)
Adenocarcinoma (solid)
Adenocarcinoma (anaplastic)
Squamous metaplastic carcinoma
Adeno- and squamous metaplastic carcinoma (mix)
Minimal lesions with discohesive cells
ILC (classic)
ILC (tubular)
ILC (solid)
ILC and squamous metaplastcic carcinoma (mix)
ILC and sarcomatoid tumour (mix)
Sarcomatoid tumour
D
Lung cancer
Co-alteration frequency (%)
KRAS
ERBB2
MYC
PIK3CA
PTEN
TP53
RE + Fusion (n = 90)
SV + Intergenic + Internal (n = 32)
E
Breast cancer
RE + Fusion (n = 30)
SV + Intergenic (n = 5)
F
Bladder cancer
RE + Fusion (n = 124)
SV + Intergenic (n = 15)
G
Pan-cancer
RE + Fusion (n = 627)
SV + Intergenic + Internal + Partial-amp (n = 126)
H
Wild-type
Mammary tumor-specific survival (%)
Months after injection
Fgfr3ΔE18 (n = 14)
Fgfr3ΔE18-Tacc3 (n = 15)
Fgfr3ΔE18-Tacc3CC1-Pro (n = 6)
Fgfr3ΔE18-Tacc3CC2-Pro (n = 6)
P < 0.0001
P = 0.0478
P = 0.2386
P = 0.0007
P < 0.0001
P = 0.1573
I
Wild-type
Mammary tumor-specific survival (%)
Months after injection
Fgfr3FL (n = 9)
Fgfr3ΔE18-Tacc3 (n = 15)
Fgfr3ΔE18-Tacc3E10-E16 (n = 9)
Fgfr3ΔE18-Tacc3S764A (n = 10)
Fgfr3ΔE18-Tacc3L772A/L773A (n = 10)
P ≤ 0.0001
P = 0.7293
P = 0.3168
P = 0.0642
P = 0.5464
P = 0.1232
P = 0.7102

Supplementary Figure S5. Mammary tumor-specific survival and histological examinations of wild-type mice intraductally injected with *Fgfr3* variants, and co-mutational context of *FGFR3* E18 truncations.

A, Kaplan-Meier curves showing mammary tumor-specific survival of female wild-type mice intraductally injected with lentiviruses encoding indicated *Fgfr3* variants. $Fgfr3^{FL}$, *n* = 9; $Fgfr3^{\Delta E18}$, *n* = 14; $Fgfr3^{FL}$-*Tacc3*, *n* = 9; $Fgfr3^{\Delta E18}$-*Tacc3*, *n* = 15; $Fgfr3^{\Delta E18}$-*K502R-Tacc3*, *n* = 4 mice. **B,** Kaplan-Meier curves showing mammary tumor-specific survival of female *Wap-Cre*;$Cdh1^{F/F}$ mice intraductally injected with lentiviruses encoding indicated *Fgfr3* variants. $Fgfr3^{FL}$, *n* = 11; $Fgfr3^{\Delta E18}$, *n* = 11; $Fgfr3^{FL}$-*Tacc3*, *n* = 11; $Fgfr3^{\Delta E18}$-*Tacc3*, *n* = 10 mice. **C,** Mammary tumor type classifications of *Fgfr3* somatic mouse models based on H&E and E-cadherin immunohistochemistry (IHC) stainings. Cohort counts (*n*) represent evaluated mammary glands per number of mice. **D-G,** Enrichment of co-alterations in key tumor driver genes (*KRAS*, *ERBB2*, *MYC*, *PIK3CA*, *PTEN*, and *TP53*) across the indicated *FGFR3* E18-truncating alteration categories in the FMI lung (**D**), breast (**E**), bladder (**F**), and pan-cancer (**G**) cohorts. SV, short variants. **H,** Kaplan-Meier curves showing mammary tumor-specific survival of female wild-type mice intraductally injected with lentiviruses encoding indicated *Fgfr3* variants. $Fgfr3^{\Delta E18}$, *n* = 14; $Fgfr3^{\Delta E18}$-*Tacc3*, *n* = 15; $Fgfr3^{\Delta E18}$-$Tacc3^{CC1\text{-}Pro}$, *n* = 6; $Fgfr3^{\Delta E18}$-$Tacc3^{CC2\text{-}Pro}$, *n* = 6 mice. **I,** Kaplan-Meier curves showing mammary tumor-specific survival of female wild-type mice intraductally injected with lentiviruses encoding indicated *Fgfr3* variants. $Fgfr3^{FL}$, *n* = 9; $Fgfr3^{\Delta E18}$-*Tacc3*, *n* = 15; $Fgfr3^{\Delta E18}$-$Tacc3^{E10\text{-}E16}$, *n* = 9; $Fgfr3^{\Delta E18}$-$Tacc3^{S764A}$, *n* = 10; $Fgfr3^{\Delta E18}$-$Tacc3^{L772A/L773A}$, *n* = 10 mice. The $Fgfr3^{\Delta E18}$ curve in (**H**), the $Fgfr3^{FL}$ curve in (**I**), and the $Fgfr3^{\Delta E18}$-*Tacc3* curves in (**H, I**) are duplicated from (**A**). *P* values in (**A, B, H, I**) were calculated using log-rank (Mantel-Cox) tests.

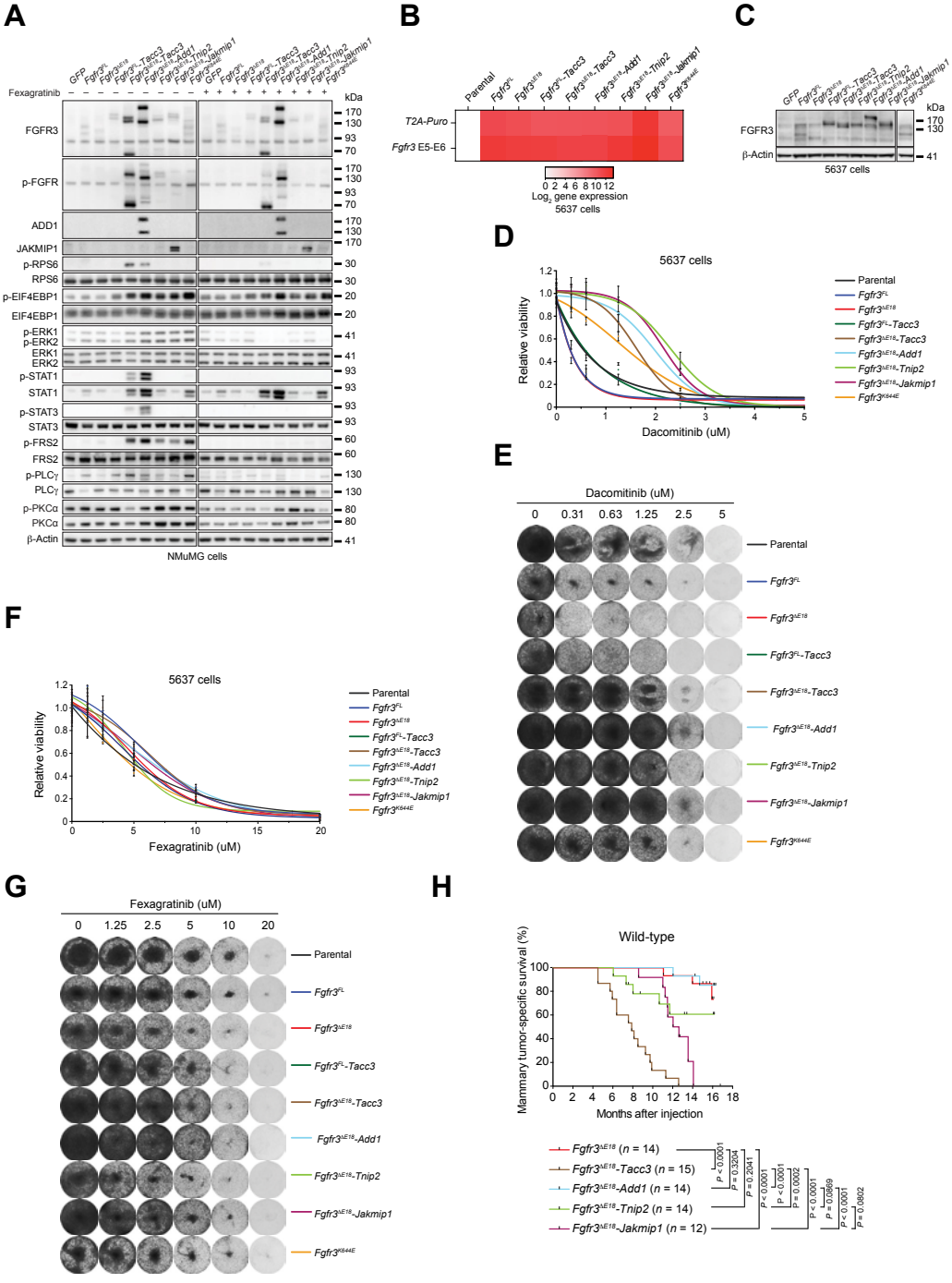
A
B
C
D
E
F
G
H
NMuMG cells
5637 cells
Fexagratinib (uM)
Dacomitinib (uM)
Relative viability
Mammary tumor-specific survival (%)
Months after injection
Wild-type
Parental
Fgfr3FL
Fgfr3LE18
Fgfr3FL-Tacc3
Fgfr3LE18-Tacc3
Fgfr3LE18-Add1
Fgfr3LE18-Tnip2
Fgfr3LE18-Jakmip1
Fgfr3K644E
Fgfr3LE18 (n = 14)
Fgfr3LE18-Tacc3 (n = 15)
Fgfr3LE18-Add1 (n = 14)
Fgfr3LE18-Tnip2 (n = 14)
Fgfr3LE18-Jakmip1 (n = 12)

Supplementary Figure S6. Functional *in vitro* and *in vivo* characterization of *Fgfr3*$^{\Delta E18}$-*Add1*, *Fgfr3*$^{\Delta E18}$-*Tnip2*, and *Fgfr3*$^{\Delta E18}$-*Jakmip1* fusions.

A, Western blots showing expression and phosphorylation of the indicated proteins in NMuMG cells stably expressing *GFP*, *Fgfr3*^{FL}, *Fgfr3*$^{\Delta E18}$, *Fgfr3*^{FL}-*Tacc3*, *Fgfr3*$^{\Delta E18}$-*Tacc3*, *Fgfr3*$^{\Delta E18}$-*Add1*, *Fgfr3*$^{\Delta E18}$-*Tnip2*, *Fgfr3*$^{\Delta E18}$-*Jakmip1* or *Fgfr3*^{K644E}, and treated for 3 hr with either vehicle or 1 μM fexagratinib following serum starvation for 24 hr. Intermediate lanes containing samples not relevant to this figure were removed for clarity. A gap indicates where the blot was cropped; samples shown were run on two different gels but imaged together and processed under identical conditions. No other alterations were made. **B,** Validation of the overexpression of *Fgfr3* variants in the 5637 bladder cancer cells using RT-qPCR. T2A–Puro primers specifically detect *Fgfr3* transcripts derived from lentiviral constructs, *Fgfr3* E4–E5 primers (spanning the exon junction of exons 4 and 5 of Fgfr3) detect both endogenous transcripts and those derived from lentiviral constructs. Log2-transformed expression of each cDNA segment is normalized to *Usf1* housekeeping gene expression. Data are represented as mean of $n = 3$ technical replica per group of 1 experiment. **C,** Western blots showing FGFR3 protein expression in the 5637 cells stably expressing *GFP*, *Fgfr3*^{FL}, *Fgfr3*$^{\Delta E18}$, *Fgfr3*^{FL}-*Tacc3*, *Fgfr3*$^{\Delta E18}$-*Tacc3*, *Fgfr3*$^{\Delta E18}$-*Add1*, *Fgfr3*$^{\Delta E18}$-*Tnip2*, *Fgfr3*$^{\Delta E18}$-*Jakmip1*, or *Fgfr3*^{K644E}. **D,** Dose-response curves of 5637 cells (either untransduced parental or transduced with lentiviruses encoding the indicated *Fgfr3* variants), treated for 3 days with dacomitinib. Cell viability was determined using CellTiter-Blue. Data were normalized to untreated conditions within each cell line and are presented as mean ± SD of $n = 2$ independent replica from 1 representative experiment. Assays were performed at least 2 times. **E,** Representative well images of (**D**), obtained after fixing and staining the cells with crystal violet. **F,** Dose-response curves of 5637 cells as in (**D**), treated for 3 days with fexagratinib. **G,** Representative well images of (**F**). **H,** Kaplan-Meier curves showing mammary tumor-specific survival of female wild-type mice intraductally injected with lentiviruses encoding indicated *Fgfr3* variants. *Fgfr3*$^{\Delta E18}$, $n = 14$; *Fgfr3*$^{\Delta E18}$-*Tacc3*, $n = 15$; *Fgfr3*$^{\Delta E18}$-*Add1*, $n = 14$; *Fgfr3*$^{\Delta E18}$-*Tnip2*, $n = 14$; *Fgfr3*$^{\Delta E18}$-*Jakmip1*, $n = 12$ mice. The *Fgfr3*$^{\Delta E18}$ and the *Fgfr3*$^{\Delta E18}$-*Tacc3* curves are duplicated from Supplementary Fig. S5A. *P* values were calculated using log-rank (Mantel-Cox) tests. In (**A**, **C**), β-Actin was run as sample processing control, blots were stained with Ponceau S to ensure equal loading of total protein, and molecular weights of protein marker bands are indicated in kDa.

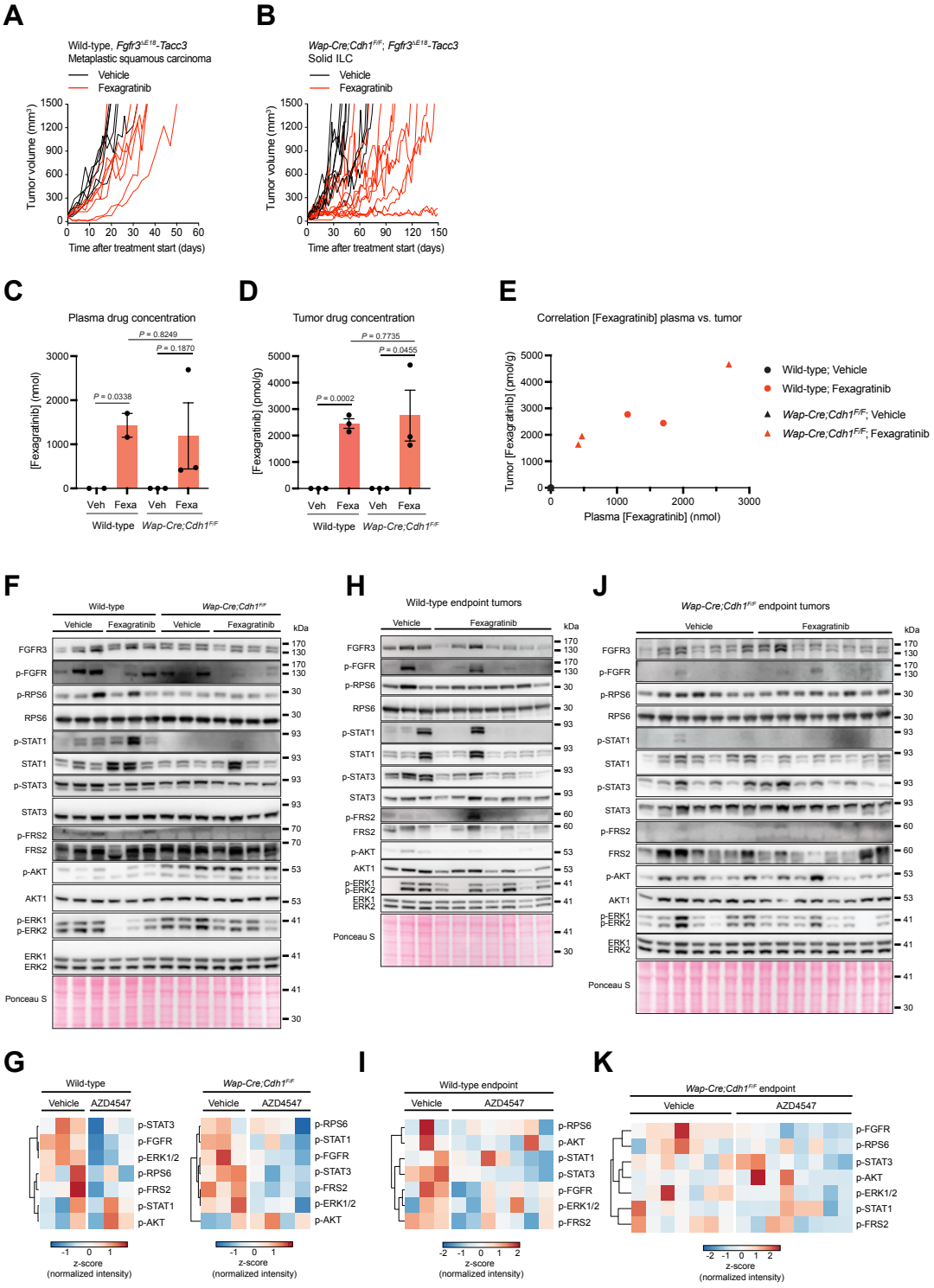
A
Wild-type, Fgfr3^1E18-Tacc3
Metaplastic squamous carcinoma
Vehicle
Fexagratinib
Tumor volume (mm³)
Time after treatment start (days)
B
Wap-Cre;Cdh1^F/F; Fgfr3^1E18-Tacc3
Solid ILC
Vehicle
Fexagratinib
Tumor volume (mm³)
Time after treatment start (days)
C
Plasma drug concentration
[Fexagratinib] (nmol)
P = 0.8249
P = 0.1870
P = 0.0338
Veh Fexa Veh Fexa
Wild-type
Wap-Cre;Cdh1^F/F
D
Tumor drug concentration
[Fexagratinib] (pmol/g)
P = 0.7735
P = 0.0455
P = 0.0002
Veh Fexa Veh Fexa
Wild-type
Wap-Cre;Cdh1^F/F
E
Correlation [Fexagratinib] plasma vs. tumor
Tumor [Fexagratinib] (pmol/g)
Plasma [Fexagratinib] (nmol)
Wild-type; Vehicle
Wild-type; Fexagratinib
Wap-Cre;Cdh1^F/F; Vehicle
Wap-Cre;Cdh1^F/F; Fexagratinib
F
Wild-type
Wap-Cre;Cdh1^F/F
Vehicle
Fexagratinib
kDa
FGFR3
p-FGFR
p-RPS6
RPS6
p-STAT1
STAT1
p-STAT3
STAT3
p-FRS2
FRS2
p-AKT
AKT1
p-ERK1
p-ERK2
ERK1
ERK2
Ponceau S
H
Wild-type endpoint tumors
Vehicle
Fexagratinib
kDa
FGFR3
p-FGFR
p-RPS6
RPS6
p-STAT1
STAT1
p-STAT3
STAT3
p-FRS2
FRS2
p-AKT
AKT1
p-ERK1
p-ERK2
ERK1
ERK2
Ponceau S
J
Wap-Cre;Cdh1^F/F endpoint tumors
Vehicle
Fexagratinib
kDa
FGFR3
p-FGFR
p-RPS6
RPS6
p-STAT1
STAT1
p-STAT3
STAT3
p-FRS2
FRS2
p-AKT
AKT1
p-ERK1
p-ERK2
ERK1
ERK2
Ponceau S
G
Wild-type
Vehicle
AZD4547
p-STAT3
p-FGFR
p-ERK1/2
p-RPS6
p-FRS2
p-STAT1
p-AKT
z-score
(normalized intensity)
Wap-Cre;Cdh1^F/F
Vehicle
AZD4547
p-RPS6
p-STAT1
p-FGFR
p-STAT3
p-FRS2
p-ERK1/2
p-AKT
z-score
(normalized intensity)
I
Wild-type endpoint
Vehicle
AZD4547
p-RPS6
p-AKT
p-STAT1
p-STAT3
p-FGFR
p-ERK1/2
p-FRS2
z-score
(normalized intensity)
K
Wap-Cre;Cdh1^F/F endpoint
Vehicle
AZD4547
p-FGFR
p-RPS6
p-STAT3
p-AKT
p-ERK1/2
p-STAT1
p-FRS2
z-score
(normalized intensity)

Supplementary Figure S7. Tumor growth response, target engagement, and adaptive resistance following fexagratinib treatment in *Fgfr3*$^{\Delta E18}$-*Tacc3*-driven mouse mammary tumors.

A, B, Individual growth curves of indicated tumor donors transplanted into the mammary fat pad of female syngeneic wild-type **(A)** or *Wap-Cre;Cdh1*$^{F/F}$ **(B)** mice and treated daily orally with vehicle or 12.5 mg/kg fexagratinib using an intermittent dosing regimen. **C,** Drug concentration in plasma of vehicle- and fexagratinib-treated mice. Each dot represents an individual mouse; bars indicate mean ± SEM. Veh, vehicle; Fexa, fexagratinib. **D,** Fexagratinib concentration in the tumor tissue of the same animals. Statistical comparisons in (**C, D**) were performed using an unpaired two-tailed t-test. **E,** Correlation between plasma and tumor drug concentrations in the two donor-derived mouse cohorts shown in (**C, D**). Each dot/triangle represents a paired measurement from an individual mouse. **F,** Western blots showing expression and phosphorylation of indicated proteins in mammary tumors from wild-type and *Wap-Cre;Cdh1*$^{F/F}$ donors treated for 2 or 5 days with vehicle or 12.5 mg/kg/day fexagratinib. **G,** Quantifications of indicated phosphoprotein band intensities based on Western blots in (**F**). Data from 2- and 5-day treatment groups in (**C-G**) were combined for clarity, as no significant differences were observed in FGFR3 signaling or fexagratinib concentrations in plasma and tumor between the two time points. **H,** Western blots showing expression and phosphorylation of indicated proteins in vehicle and fexagratinib-treated outgrown endpoint mammary tumors from a wild-type donor. **I,** Quantifications of indicated phosphoprotein band intensities based on Western blots in (**H**). **J,** Western blots showing expression and phosphorylation of indicated proteins in vehicle and fexagratinib-treated outgrown endpoint mammary tumors from a *Wap-Cre;Cdh1*$^{F/F}$ donor. **K,** Quantifications of indicated phosphoprotein band intensities based on Western blots in (**J**). Ponceau S staining is shown as a total protein loading control in (**F**, **H** and **J**). In (**G**, **I**, **K**), phospho band intensities were normalized to their corresponding total protein band intensities and β-actin bands. Values were then normalized to vehicle-treated controls and variance-scaled across samples.